

The use of remote sensing for reliable estimation of net radiation and its components: a case-study for contrasting land covers in an agricultural hotspot of the Brazilian semiarid region

Article

Accepted Version

Creative Commons: Attribution-Noncommercial-No Derivative Works 4.0

Ferreira, T. R., da Silva, B. B., de Moura, M. S. B., Verhoef, A. ORCID: <https://orcid.org/0000-0002-9498-6696> and Nobrega, R. L. B. (2020) The use of remote sensing for reliable estimation of net radiation and its components: a case-study for contrasting land covers in an agricultural hotspot of the Brazilian semiarid region. *Agricultural and Forest Meteorology*, 291. 108052. ISSN 0168-1923 doi: <https://doi.org/10.1016/j.agrformet.2020.108052> Available at <https://centaur.reading.ac.uk/90838/>

It is advisable to refer to the publisher's version if you intend to cite from the work. See [Guidance on citing](#).

To link to this article DOI: <http://dx.doi.org/10.1016/j.agrformet.2020.108052>

Publisher: Elsevier

including copyright law. Copyright and IPR is retained by the creators or other copyright holders. Terms and conditions for use of this material are defined in the [End User Agreement](#).

www.reading.ac.uk/centaur

CentAUR

Central Archive at the University of Reading

Reading's research outputs online

1 **The use of remote sensing for reliable estimation of net radiation and its**
2 **components: a case-study for contrasting land covers in an agricultural**
3 **hotspot of the Brazilian semiarid region**

4 **Thomás R. Ferreira^{1,*}, Bernardo B. da Silva¹, Magna S. B. de Moura², Anne Verhoef³ and**
5 **Rodolfo L. B. Nóbrega^{3,4}**

6 ¹ Federal University of Campina Grande, Av. Aprígio Veloso, 822, Cidade Universitária, CEP
7 58420-102, Campina Grande, PB, Brazil

8 ² Brazilian Agricultural Research Corporation, Embrapa Tropical Semi Arid, BR 428, Km 152, s/n,
9 Zona Rural, CEP 56302-970, Petrolina, PE, Brazil

10 ³ The University of Reading, Whiteknights, Reading RG6 6AB, United Kingdom

11 ⁴ Imperial College London, Department of Life Sciences, Ascot SL5 7PY, United Kingdom

12 * Correspondence to: thomas.ferreira@ufcg.edu.br; Tel.: +55-083-2101-1202

13
14 **Abstract:** This study aims to ascertain the uncertainties related to the spatiotemporal estimation of
15 net radiation, and its components, using remote sensing data. Geographical focus is an irrigated
16 agricultural hotspot of the Brazilian semiarid region, for which we also investigate the impact that
17 contrasting land-cover types have on the upwelling radiation balance components, and hence on net
18 radiation. Instantaneous (R_n) and daily ($R_{n,24}$) values of net radiation were estimated based on
19 OLI/TIRS-Landsat-8 images and key weather variables. In addition, we evaluated two models for
20 downwelling shortwave (R_{sw}), ten models for downwelling longwave radiation (R_{lw}), and two
21 models for derivation of $R_{n,24}$. The accuracy of each model was evaluated with radiation
22 measurements obtained from research quality sensors installed in micrometeorological towers. The
23 best performances were found for the Allen model, Duarte model, and De Bruin model for R_{sw} , R_{lw} ,
24 and $R_{n,24}$, respectively. The contrasting land-use types exhibited substantial differences in the
25 biophysical variables and radiative properties that affect R_n . The albedo for the irrigated crops has
26 average absolute values that are 0.01–0.03 larger than those found for the pristine caatinga, whereas

27 the land surface temperature, LST, is 3–5 degrees smaller. However, R_n for these two distinctly
28 different surface types was similar, as a result of a considerably lower surface emissivity in the
29 caatinga. For rangeland, the albedo, LST, and hence the upwelling radiation had greater values than
30 those found for the caatinga, which caused reduced values of R_n . The urban areas exhibited the
31 lowest values of R_n , mainly as a consequence of their high albedo values. We show that when in-situ
32 net radiation data are not available, remote sensing data combined with more readily available in-situ
33 weather data can be used to derive spatiotemporal estimates of R_n . This facilitates the identification
34 of anthropogenic impacts on the radiation at the land-surface and ultimately the energy balance,
35 including the short-term seasonal and long-term effects.

36 **Keywords:** remote sensing; land use change; caatinga; energy balance; longwave radiation;
37 downwelling solar radiation.

38 1. Introduction

39 The Brazilian semiarid region is predominantly characterized by the Caatinga, a seasonally dry
40 tropical forest, which is ecologically rich. Few studies have addressed the effects of anthropogenic
41 changes on this natural vegetation cover, especially in the context of land-surface climate interactions
42 (e.g. Cunha et al., 2020; Marques et al., 2020). During the past decades, the Caatinga has been
43 extensively affected by anthropogenic land-cover changes, and only a few ecologically important
44 landscapes of this natural habitat remain, of which only 1.3% is protected by law (CNUC/MMA,
45 2018). This region is the most populous semiarid territory in the world (IBGE, 2010), and yet one of
46 the most threatened Brazilian natural landscapes; mainly because it comprises originally pristine
47 Caatinga areas that are now affected by desertification, agricultural intensification (both rainfed and
48 irrigated crops), and (over)grazing (pasture). Most of water resources in this region come from the
49 São Francisco River, whose waters supply several municipalities; for human consumption, generation
50 of energy and agricultural activity. The increase of irrigated agriculture in the Caatinga, in particular
51 during recent years, has had positive socio-economic implications but it has also increased conflicts
52 related to water use.

53 The anthropogenic activities influence local climate through changes in surface properties and
54 state variables such as albedo and land-surface temperature (Bonan 2008; Gomes et al., 2009;
55 Kvalevag et al., 2010; Li et al., 2019). Therefore, the local and regional atmospheric circulation in the
56 Caatinga has being affected (Correia et al., 2006; Melo et al., 2015). These alterations in biophysical
57 surface variables impact the surface net radiation balance, as observed by Silva et al. (2015) who
58 studied the replacement of woody savanna by agricultural crops and eucalyptus plantation, and by Liu
59 et al. (2019) who investigated the radiative effects of the conversion of croplands to grasslands.

60 Net radiation (R_n) is defined as the balance between incoming (downwelling) and outgoing
61 (upwelling) shortwave and longwave radiation at the surface. The downwelling fluxes are strongly
62 dependent on latitude, solar angle (for shortwave radiation), as well as cloudiness and atmospheric
63 properties such as temperature and vapour pressure, that affect the longwave downwelling flux
64 directly (i.e., air temperature, via Stefan Boltzmann's law) or indirectly through changes in
65 atmospheric emissivity. Important variables for the upwelling radiation fluxes are albedo (shortwave
66 radiation), and land surface temperature and surface emissivity, that together determine the longwave
67 upwelling radiation, again calculated by Stefan Boltzmann's law. All of these atmospheric and surface
68 variables display considerable spatial and temporal variability, which directly affect heat and mass
69 exchanges in the planetary boundary layer (Silva et al., 2015; Kilic et al., 2016).

70 Estimation of R_n is very important in the context of turbulent energy flux estimates (latent heat
71 flux (i.e., evapotranspiration), and sensible heat flux), particularly in those studies devoted to the
72 assessment of evapotranspiration based on remote sensing techniques (Bastiaanssen et al., 1998, 2005;
73 Allen et al., 2007; Silva et al., 2015; Elnmer et al., 2019) and those employing the Bowen ratio
74 method, where R_n (as a key component of the available energy) is crucial for the reliable calculation
75 of latent and sensible heat fluxes (Verhoef and Campbell, 2005). Reliable values of R_n are also
76 required to check the closure of the energy balance when turbulent energy fluxes have been directly
77 determined with the eddy covariance technique, because there may be an underestimation due to the
78 existence of storage of heat in canopies or in the layer below the instrumentation, horizontal
79 advection, errors in the frequency response of sensors, and regional scale heterogeneity that can cause
80 large-scale eddies that are not readily sensed by eddy covariance systems. Therefore, the sum of

81 measured latent plus sensible heat fluxes needs to be compared with values of net radiation minus
82 ground heat flux, to assess the magnitude of the non-closure (Jensen and Allen, 2016). R_n can be
83 directly determined onsite with net radiometers, which are accurate but expensive and only produce
84 measurements representative of relatively small areas (Jensen and Allen, 2016).

85 Satellite imagery has been widely used to determine R_n from field to regional scales, and over
86 heterogeneous areas (Bisht et al., 2005; Allen et al., 2007; Ryu et al., 2008; Bisht and Bras, 2010;
87 Silva et al., 2011; Silva et al., 2015). In this context, various algorithms have been developed to
88 estimate the downwelling shortwave radiation (Zillman, 1972; Allen et al., 2007), downwelling
89 longwave radiation (Sugita and Brutsaert, 1993; Prata, 1996; Bastiaanssen et al., 1998; Duarte et al.,
90 2006; Allen et al., 2007; Kruk et al., 2010; Santos et al., 2011), longwave radiation balance, and
91 radiative properties such as surface emissivity (Tasumi, 2003; Muñoz-Jiménez et al., 2006; Tang and
92 Li, 2008; Teixeira et al., 2009).

93 For the downwelling shortwave radiation, Bisht et al. (2005), Bisht and Bras (2010), Alados et al.
94 (2011) and Silva et al. (2015) in subtropical regions, and Vancoppenolle et al. (2011) in Antarctica,
95 have obtained good results when applying the model proposed by Zillman (1972). On the other hand,
96 the Mapping Evapotranspiration at High Resolution with Internalized Calibration (METRIC) model
97 employed by Allen et al. (2007), ensured that for clear sky conditions, the accuracy of METRIC
98 downwelling shortwave radiation was comparable to data measured with a pyranometer sensor
99 mounted on an automated weather station (Allen 1996; ASCE-EWRI 2005; Jensen and Allen, 2016).

100 Several models are dedicated to estimate the downwelling longwave radiation; Allen et al.
101 (2007), Allen et al. (2011), and Santos et al. (2020) recommend the expression employed in
102 Bastiaanssen et al. (1998). Silva et al. (2015) evaluated nine models of downwelling longwave
103 radiation at the Mogi Guaçu watershed (a subtropical Brazilian basin), and found that the model of
104 Duarte et al. (2006) presented the best performance on the basis of mean errors. Other studies also
105 indicated a good performance of the Duarte et al. (2006) model (in Korea: Choi, 2013; in the Brazilian
106 southeastern region: Kruk et al., 2010; and in Argentina: Carmona et al., 2014). Santos et al. (2011)
107 proposed a model that showed errors less than 1.0%, in a banana orchard located in the semiarid
108 region of Northeast Brazil.

109 Regarding daily net radiation, Bastiaanssen et al. (2000) recommended the use of the expression
110 employed by De Bruin (1987) in remote sensing applications (in this case Landsat images were
111 employed). Silva et al. (2015), when using this model with TM Landsat 5 images, found small mean
112 errors, at the Mogi Guaçu watershed (mentioned above), in a sugarcane field and in a Cerrado forest
113 area. Trigo et al. (2018) successfully validated a Priestley-Taylor (Priestley and Taylor, 1972) grass
114 reference evapotranspiration product (that uses a Meteosat Second Generation shortwave radiation
115 product, and the De Bruin (1987) equation), in a non-irrigated grass area (Cabauw, The Netherlands),
116 and showed a modest bias of -0.4 mm/day. Another method to obtain daily net radiation was
117 developed by Bisht et al. (2005); it has been used in several remote sensing studies (Bisht and Bras,
118 2010; Bisht and Bras, 2011; Ruhoff et al., 2012; Zhu et al., 2017; Wang et al., 2019).

119 However, there is a lack of applications and validation of those models in the framework of the
120 assessment of the effect of land-cover change on land-surface radiation components for Brazilian
121 semiarid conditions. A better quantification of regional net radiation for evapotranspiration estimates
122 will provide reliable information to decision makers for a more efficient management of water
123 resources. Hence, the aims of this study are: (a) to assess the uncertainties related to the estimation of
124 net radiation components from remote sensing methods, and (b) to evaluate the impact that
125 contrasting land-cover types have on the radiation balance components in an agricultural hotspot of
126 the Brazilian semiarid region, using remote sensing and in-situ data. This is the first study of its kind
127 in this region.

128 **2. Materials and Methods**

129 *2.1 Study area: Climatology and land use (sampling)*

130 The study area is located in the Brazilian Caatinga domain, an area that originally encompassed
131 approximately 900,000 km². Over the past decades large pristine Caatinga areas have been cleared
132 and replaced by rainfed (mostly) and irrigated agriculture, while in other areas grasses took over and
133 grazing pasture became the dominant land-cover type. Within the Caatinga, we selected an area of
134 7,366 km², which is situated in the Low-Middle São Francisco river watershed, between the federal
135 states of Pernambuco (PE) and Bahia (BA). The selected area includes part of the São Francisco

136 River, urban areas of Petrolina and Juazeiro towns, Caatinga and pasture vegetation, and irrigated
137 crops (about 70,000 hectares) (Fig. 1). Although irrigated agriculture is not the most common type of
138 agriculture found in the Brazilian semiarid region, it is predominant in the area of study due to the
139 easy access to the São Francisco river, that supplies the irrigation water. The land-use data were
140 produced by MapBiomas (Projeto MapBiomas, 2019), that uses automatic classification procedures
141 applied to satellite images to generate coverage and land-use data. Note that information on rainfed
142 agricultural land use is not available in MapBiomas (most likely because the rainfed areas are too
143 small in that region to be detected by Landsat), hence this land use was not considered in our study.
144 The climatology for Petrolina is presented in Table S1 for the 1981–2010 period, the procedures for
145 obtaining it are in accordance with World Meteorological Organization WMO technical
146 recommendations (WMO station code: 81991; WMO; 1989; INMET, 2018).

147 With the aim to evaluate the impact that land-use changes have had/could have on the land
148 surface state variables and the radiation balance of the original Brazilian Caatinga, we selected 100
149 random data points (for the variables given below) for caatinga vegetation, irrigated agriculture,
150 pasture, and urban infrastructure (i.e., a total of 400 points). This procedure provided a common basis
151 for comparison between the landcover types, using the same spatial sampling structure, and followed
152 the methodology of other studies (e.g. Reynolds et al, 2006; Lin et al., 2014; Robinson et al., 2017;
153 Hoagland et al., 2018). The random points were generated for each land-use type using a random
154 points tool of QGIS 3.6 Noosa (QGIS, 2020), a reliable and practical tool also utilized in other studies
155 (Waldmann-Selsam et al., 2016; Wijesingha et al., 2019; Urrutia et al., 2020), that helps avoid bias.
156 These data were used to create box-plots for land surface temperature (LST), net radiation at the time
157 of satellite overpass ($R_{n,over}$, see Eq. 1), Normalized Difference Vegetation Index – NDVI (Rouse et
158 al., 1974) albedo, and surface emissivity ϵ_0 , based on MapBiomas classification
159 (<http://mapbiomas.org>), (Fig. 1).

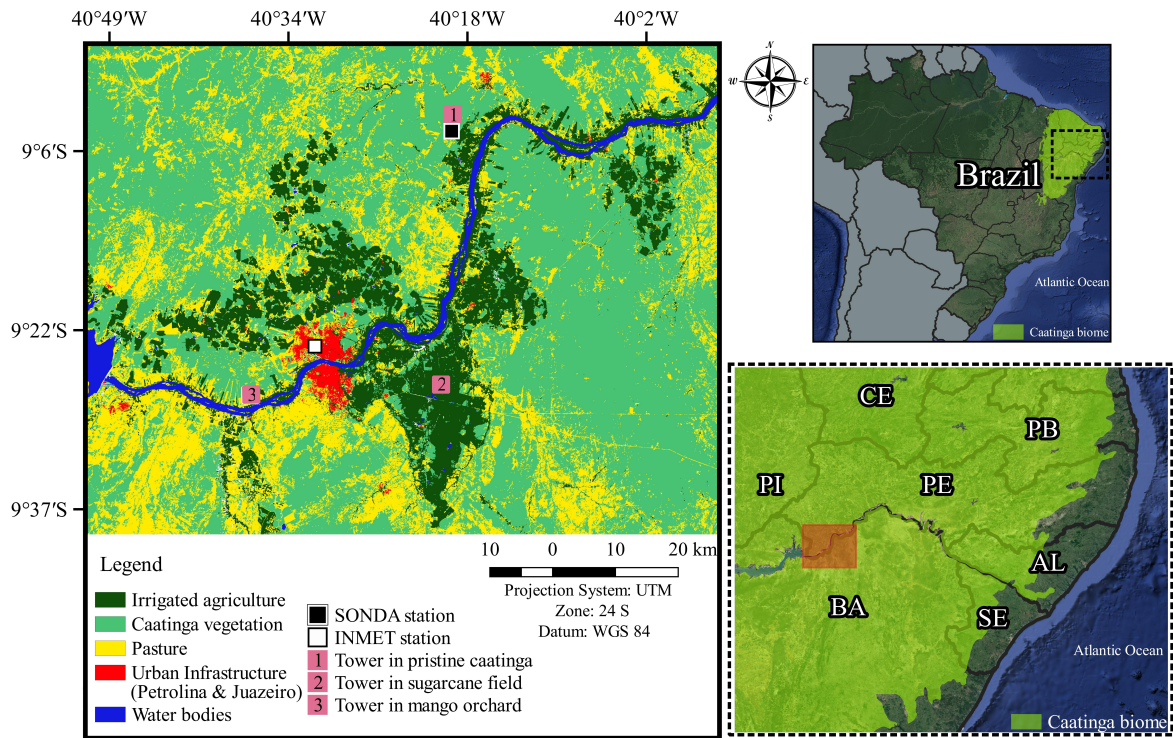


Figure 1. Coverage and land use map of the study area. The subsets indicate the four contrasting land-cover types that were studied. Data were obtained from ‘Projeto MapBiomias’.

160

161 The maximum daily air temperature (T_{\max}), of the study area (see Table S1) ranges from 29.7 °C
 162 (July) to 34.2 °C (November), with an annual mean of 32.3 °C. The mean annual minimum air
 163 temperature (T_{\min}) is 22.2 °C, and varies between 20.0 °C (July) and 23.5 °C (December). The mean
 164 daily sunshine hours duration varies from 7.3 h (June) to 9.2 h (September–October). Mean monthly
 165 rainfall ranges between 1.4 mm (August) to 114.1 mm (March); most of this (70.4%) falls between
 166 January and April with an annual mean of 482.6 mm (See Table S1 in the supplementary material).
 167 The high values of daily downwelling shortwave radiation (up to 36 MJ m⁻²), low values of air
 168 relative humidity (from 43.8% in October to 60.2% in June), and relatively high wind speeds (~ 3 m s⁻¹
 169 on average) result in an annually averaged Class A pan evaporation of 9.2 mm day⁻¹, with
 170 accumulated monthly values ranging between 216.8 mm (April) and 387.8 mm (October). The annual
 171 reference evapotranspiration (ET_0) for the 30-year period is 1887 mm. Based on these data the local
 172 climate can be classified as semi-arid to arid.

173

174 *2.2 Satellite images and weather data*

175 We used the Operational Land Imager (OLI) Collection 1 Level-1 bands 2 (0.450–0.51 μm), 3
176 (0.53–0.59 μm) and 4 (0.64–0.67 μm) in the visible spectrum, 5 (0.85–0.88 μm) in the near-infrared,
177 6 (1.57–1.65 μm) and 7 (2.11–2.29 μm) in the shortwave infra-red, all with a spatial resolution of 30
178 m, as well as the Thermal Infrared Sensor (TIRS) band 10 with a spatial resolution of 100 m. We used
179 thirty OLI/TIRS Landsat 8 images, path 217 and rows 66 and 67, for the period from 2013-2019 (for
180 the dates and times of the satellite overpass, see the first column in Table S2) (USGS, 2018). We used
181 the Level-1 Quality Assessment product of Landsat 8 to ensure that no bad satellite data were
182 included in the processing.

183 One-minute data of air temperature— T_a ($^{\circ}\text{C}$), relative humidity—RH (%), atmospheric
184 pressure— P_a (kPa), downwelling shortwave radiation— $R_{\text{sw,obs}}$ (W m^{-2}), and downwelling longwave
185 radiation— $R_{\text{lw,obs}}$ (W m^{-2}) were obtained from Petrolina Station (hereinafter referred to as SONDA
186 station; part of the Baseline Surface Radiation Network (BSRN)). For details of sensors and data
187 quality control see Driemel et al. (2018). For the present study, we used the one-minute data at the
188 satellite overpass times (Table S2) to calculate variables required for the calculation of $R_{\text{n,over}}$.

189 Measurements from 4-component net radiometers (CNR1 model Kipp-Zonen, Delft, the
190 Netherlands), installed in a micrometeorological tower (at 8 m height) in irrigated sugarcane (SC), in
191 irrigated mango orchard (MO), at 6 m, and at 14 m in a pristine caatinga (PC) (Fig. 1), were used to
192 validate the instantaneous and daily R_n results derived from OLI/TIRS Landsat 8 images. Ten images
193 (2013–2015) were used for SC (in-situ R_n data were not available for the other five days for which
194 images were available during this period), eight (2017-2019) for MO (in-situ R_n data were not
195 available for the other four days) and sixteen (2015–2019) for PC (in-situ R_n data were not available
196 for the other six days). The CNR1 measurements were collected every 30 seconds, and averages were
197 recorded at 30-minute (SC and PC) and 10-minute (MO) intervals by a datalogger (CR23X for
198 sugarcane, CR1000 for Caatinga, and CR5000 for mango orchard, manufactured by Campbell
199 Scientific., Logan, UT, USA).

200 *2.3 Determination of instantaneous net radiation*

201 The *instantaneous* net radiation at the surface during the satellite overpass— $R_{n,over}$ ($W\ m^{-2}$) was
 202 calculated using Eq. 1 (Allen et al., 2007; Silva et al., 2015):

$$R_{n,over} = (1 - \alpha)R_{sw} - R_{emi} + \varepsilon_0 R_{lw} \quad (1)$$

203 where α (dimensionless) is the surface broadband albedo (dimensionless), R_{sw} ($W\ m^{-2}$) is the
 204 downwelling shortwave radiation (estimated by different parameterizations, subsection 2.3.2), R_{emi}
 205 ($W\ m^{-2}$) is the longwave radiation emitted by the surface, ε_0 is the pixel surface emissivity, and R_{lw} (W
 206 m^{-2}) is the downwelling longwave radiation emitted by the atmosphere, all obtained at the time of the
 207 satellite overpass.

208 The instantaneous net radiation at the surface— $R_n(t)$ ($W\ m^{-2}$) at any time t (local solar time) of
 209 the diurnal cycle (from sunrise to sunset, only for $R_n(t) > 0$) can be obtained based on the assumption
 210 that the diurnal variability of net radiation follows a sinusoidal pattern (Bisht et al., 2005):

$$R_n(t) = R_{n,max} \sin \left[\left(\frac{t - t_{rise}}{t_{set} - t_{rise}} \right) \pi \right] \quad (2)$$

211 where $R_{n,max}$ ($W\ m^{-2}$) is the maximum daily net radiation and t_{rise} and t_{set} are the times when $R_n(t)$
 212 becomes positive and negative, respectively, throughout the day (we assume that t_{rise} occurs 50
 213 minutes after sunrise and t_{set} occurs 50 minutes before sunset). $R_{n,max}$ was determined according to
 214 (Bisht et al., 2005):

$$R_{n,max} = \frac{R_{n,over}}{\sin \left[\left(\frac{t_{over} - t_{rise}}{t_{set} - t_{rise}} \right) \pi \right]} \quad (3)$$

215

216 2.3.1 Broadband albedo

217 The broadband surface albedo - α , for each pixel with atmospheric correction, was obtained
 218 according to the following expression (Bastiaanssen et al., 1998; Allen et al., 2007; Silva et al., 2016):

$$\alpha = \left(\frac{\alpha_{toa} - a}{\tau_{sw}^2} \right) \quad (4)$$

219 where α_{toa} is the broadband albedo at the top of atmosphere, i.e., before atmospheric correction, a is
 220 the atmospheric reflectance (set to 0.03, as used in many studies (Bastiaanssen et al., 2000; Silva et

221 al., 2015; Silva et al., 2016)) and τ_{sw} is the atmospheric transmissivity for clear sky conditions (see Eq.
 222 7). α_{toa} consists of a linear combination of the spectral reflectance of the six reflective OLI bands,
 223 according to Silva et al. (2016):

$$\alpha_{toa} = 0.300 r_2 + 0.277 r_3 + 0.233 r_4 + 0.143 r_5 + 0.036 r_6 + 0.001 r_7 \quad (5)$$

224 where r_2 – r_7 are the reflectivities of OLI spectral bands 2–7, respectively, each one of them obtained
 225 using Eq. 6:

$$r_b = \left(\frac{Add_b + Mult_b DN}{\cos Z dr} \right) \quad (6)$$

226 where the terms Add_b and $Mult_b$ belong to the radiometric rescaling group, specifically the
 227 reflectance_add_band (equal to -0.1) and reflectance_mult_band (equal to 0.00002), respectively,
 228 presented in the metadata of each OLI – Landsat 8 image, Z is the solar zenith angle, and dr is the
 229 relative Earth-Sun distance squared (dimensionless), see Table S2. Parameter τ_{sw} is obtained from
 230 (Allen et al., 2007):

$$\tau_{sw} = 0.35 + 0.627 \exp \left[\frac{-0,00146 P_a}{K_t \cos Z} - 0.075 \left(\frac{W}{\cos Z} \right)^{0.4} \right] \quad (7)$$

231 in which K_t is the atmospheric turbidity coefficient, P_a is atmospheric pressure (kPa; see Table 1), and
 232 W is precipitable water (mm), defined by the following equation (Garrison and Adler, 1990):

$$W = 10 \left[1.4 e_a \left(\frac{P_a}{P_{sml}} \right) + 0.21 \right] \quad (8)$$

233 where e_a is the partial pressure of atmospheric water vapor (kPa), obtained from RH and T_a measured
 234 at the SONDA site (see Table S2 and Section 2.2), P_a is the atmospheric pressure (in kPa, see Table
 235 S2), and P_{sml} is the atmospheric pressure at mean sea level (101.3 kPa).

236 2.3.2 Downwelling shortwave radiation assessment

237 The downwelling shortwave radiation— R_{sw} ($W m^{-2}$), at the satellite overpass time, for clear-sky
 238 condition was estimated by parameterizations developed by Allen et al. (2007)— $R_{sw,Aln}$ (referred to as
 239 Allen model) and Zillman (1972)— $R_{sw,Zlm}$ (referred to as Zillman model), according to the following
 240 equations:

$$R_{sw,Atm} = S_0 \cos Z d_r \tau_{sw} \quad (9)$$

$$R_{sw,zlm} = \frac{S_0 \cos^2 Z}{1.085 \cos Z + e_a (2.7 + \cos Z) 10^{-3} + \beta} \quad (10)$$

241

242 where S_0 is the solar constant (1361 W m^{-2}) and β is an adjustment coefficient that was evaluated for
 243 two different values $\beta = 0.10$ ($R_{sw,Z.1}$, originally adopted by Zillman, 1972) and $\beta = 0.2$ ($R_{sw,Z.2}$
 244 suggested by Bisht et al., 2005; Bisht et al., 2010; and Silva et al., 2015); all other symbols are as
 245 defined before.

246

247 2.3.3 Estimation of upwelling and downwelling longwave radiation

248 The upwelling longwave radiation emitted by the surface at the satellite overpass— R_{emi} (W m^{-2})
 249 was calculated according to Stefan-Boltzmann's Law:

$$R_{emi} = \varepsilon_0 \sigma LST^4 \quad (11)$$

250 where σ is the Stefan-Boltzmann constant, ε_0 is the pixel surface emissivity, and LST is the land
 251 surface temperature (K), which was obtained using the spectral radiance of band 10 of the TIRS— $L_{\lambda 10}$
 252 ($\text{W m}^{-2} \text{ sr}^{-1} \mu\text{m}^{-1}$) and the emissivity at the nearest band— ε_{NB} , through the inverted Planck Law
 253 (Markham and Barker, 1986):

$$LST = \frac{K_2}{\ln\left(\frac{\varepsilon_{NB} K_1}{L_{\lambda,10}} + 1\right)} \quad (12)$$

254

255 where K_1 and K_2 are radiation constants specific to TIRS-Landsat 8 band 10, equaling 774.89 W m^{-2}
 256 $\text{sr}^{-1} \mu\text{m}^{-1}$ and 1321.08 K , respectively. The surface emissivity across the entire longwave radiation
 257 spectrum— ε_0 and the one associated with the thermal band spectrum, ε_{NB} , were calculated based on
 258 the Leaf Area Index, LAI, according to Tasumi (2003), for each pixel.

259 The atmospheric downwelling longwave radiation— R_{lw} (W m^{-2}) was calculated using Stefan-
 260 Boltzmann's Law (analogous to Eq. 11):

$$R_{lw} = \varepsilon_a \sigma T_a^4 \quad (13)$$

261

262 where LST in Eq. 11 was substituted by T_a (K), measured at the SONDA station of Petrolina, and the
 263 surface emissivity was replaced by the atmospheric emissivity— ε_a . Parameter ε_a was determined with
 264 the expression that provided the best estimate of R_{lw} among ten different models, when compared with
 265 pyrgeometer measurements at the SONDA station. The various expressions used to compute ε_a are
 266 listed in Table 1. Note that those equations by Brutsaert (1975), Sugita and Brutsaert (1993), Duarte
 267 et al. (2006), Kruk et al. (2010), and Santos et al. (2011) are in fact the same equation but with
 268 different parameter constants. All models we tested required weather data (T_a , RH, and P_a) collected
 269 at the SONDA station at one-minute intervals (Table S2).

270

271 **Table 1.** Different models evaluated for clear-sky atmospheric emissivity— ε_a (dimensionless)
 272 determination based on atmospheric vapor pressure— e_a (hPa) and air temperature— T_a (K) data (see
 273 Table S2)

| Author(s) | Equation |
|-----------------------------|---|
| Swinbank (1963) | $\varepsilon_a = 9.365 \cdot 10^{-6} \cdot T_a^2$ |
| Idso and Jackson (1969) | $\varepsilon_a = 1 - 0.261 \exp[-7.77 \cdot 10^{-4} (273 - T_a)^2]$ |
| Brutsaert (1975) | $\varepsilon_a = 0.643 \left(\frac{e_a}{T_a}\right)^{1/7}$ |
| Idso (1981) | $\varepsilon_a = 0.70 + 5.95 \cdot 10^{-7} e_a \exp\left(\frac{1500}{T_a}\right)$ |
| Sugita and Brutsaert (1993) | $\varepsilon_a = 0.714 \left(\frac{e_a}{T_a}\right)^{0.0687}$ |
| Prata (1996) | $\varepsilon_a = \{1 - (1 + \varphi) \exp[-(1.2 + 3.0 \varphi)^{0.5}]\}$ with $\varphi = 0.465 \left(\frac{e_a}{T_a}\right)$ |
| Bastiaanssen et al. (1998) | $\varepsilon_a = 0.85(-\ln \tau_{SW})^{0.09}$ |
| Duarte et al. (2006) | $\varepsilon_a = 0.625 \left(\frac{e_a}{T_a}\right)^{0.131}$ |
| Kruk et al. (2010) | $\varepsilon_a = 0.576 \left(\frac{e_a}{T_a}\right)^{0.202}$ |
| Santos et al. (2011) | $\varepsilon_a = 0.6905 \left(\frac{e_a}{T_a}\right)^{0.0881}$ |

274 2.3.4 Daily net radiation

275 The *daily* net radiation— $R_{n,24}$ (W m^{-2}) was obtained according to De Bruin (1987) (see also
 276 Bastiaanssen et al., 2000; Silva et al., 2015):

277

$$R_{n,24,DeB} = (1 - \alpha) R_{sw,24} - 110 \tau_{sw24} \quad (14)$$

278

279 where α is the surface broadband albedo (see Eq. 4); $R_{sw,24}$ ($W m^{-2}$) is the downwelling shortwave
 280 radiation (locally measured at SONDA Station) integrated for 24 hours; and τ_{sw24} is the ratio of the
 281 daily downwelling shortwave radiation— $R_{sw,24}$ ($MJ m^{-2}$) and the daily extraterrestrial solar radiation
 282 (at the top of atmosphere)— $R_{sw,toa}$ ($MJ m^{-2}$). The second term in Eq. 14 accounts for the longwave
 283 radiation which reduces $R_{n,24}$, and the constant 110 is locally calibrated as obtained by De Bruin
 284 (1987) and applied satisfactorily by Bastiaanssen et al. (2000) and Silva et al. (2015). We also
 285 determined daily net radiation according to the sinusoidal model developed by Bisht et al. (2005)
 286 valid only for clear sky days (referred to as Bisht model):

$$R_{n,24,Bst} = \frac{2 R_{n,max}}{\pi} \quad (15)$$

287 where $R_{n,max}$ ($W m^{-2}$) is the maximum daily net radiation value, which was obtained by Eq. 3.

288

289 2.4 Statistical metrics

290

291 The performance of the results was determined by the Mean Errors (Absolute Mean Error—
 292 MAE and relative mean error—MRE), the Root Mean Square Error—RMSE, the Pearson correlation
 293 coefficient— r and the Coefficient of Residual Mass—CRM:

$$MRE = \frac{100}{n} \sum_{i=1}^n \left| \frac{X_{est} - X_{obs}}{X_{obs}} \right| \quad (16)$$

$$MAE = \frac{1}{n} \sum_{i=1}^n |X_{est} - X_{obs}| \quad (17)$$

$$RMSE = \left(\frac{\sum_{i=1}^n (X_{est} - X_{obs})^2}{n} \right)^{\frac{1}{2}} \quad (18)$$

$$r = \frac{\sum_{i=1}^n (X_{est} - \bar{X})(X_{obs} - \bar{X})}{\left[\sum_{i=1}^n (X_{est} - \bar{X})(X_{obs} - \bar{X})^2 \right]^{\frac{1}{2}}} \quad (19)$$

$$CRM = \frac{\sum_i^n (X_{obs} - X_{est})}{\sum_i^n (X_{obs})} \quad (20)$$

294 where X_{obs} , X_{est} and \bar{X} correspond to measured, estimated and averaged values of the parameterized
 295 variables (R_{lw} , R_{sw} , R_n , and $R_{n,24}$), and n corresponds to the number of observed and estimated
 296 variables.

297 3. Results and Discussion

298 3.1 Solar radiation and atmospheric transmittance

299 The atmospheric transmittance values— τ_{sw} associated with the Landsat 8 overpass times over the
 300 studied region are presented in Table S3. Values of τ_{sw} ranged between 0.723 (May 30, 2013 – DOY
 301 150) and 0.758 (Oct 5, 2013 – DOY 278), making them generally higher than the daily average
 302 transmittance— $\tau_{sw,24}$, also presented in the same table. The presence of clouds throughout the day
 303 attenuates solar radiation and, thus, reduces $\tau_{sw,24}$, which consequently reduces the daily downwelling
 304 shortwave radiation— $R_{sw,24}$. Contrasting sky conditions can be appreciated in SONDA data over
 305 different seasons (clear sky with $\tau_{sw,24} = 0.720$ – Fig. 2a and cloudy sky with $\tau_{sw,24} = 0.684$ – Fig. 2b).
 306 We had 73% of the selected dates with $\tau_{sw,24}$ higher than 0.7, representative of clear days, and 27%
 307 with $\tau_{sw,24}$ lower than 0.7 (ranging from 0.649 to 0.692), i.e. days where some clouds were present.

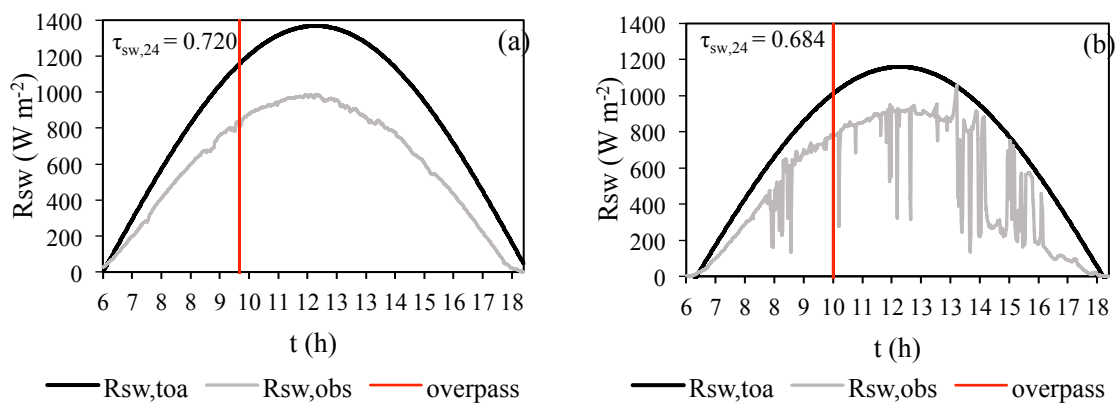


Figure 2. Downwelling shortwave radiation — $R_{sw,obs}$ ($W m^{-2}$) measured at SONDA station (Petrolina-PE; grey line), downwelling extraterrestrial solar radiation (at the top of atmosphere) — $R_{sw,toa}$ ($W m^{-2}$; black line) and time of satellite overpass (red line) for October 5, 2013 – DOY 278

(a) and May 22, 2016 – DOY 142 (b).

308 The measured instantaneous values of downwelling shortwave radiation at the SONDA station—
309 $R_{sw,obs}$ at time of satellite overpass, ranged between 704 W m^{-2} (June 2, 2014 – DOY 153) and 956 W m^{-2}
310 m^{-2} (Oct 27, 2015 – DOY 300) (Table S3). All shortwave models had MRE values smaller than 7%,
311 but the best model was the $R_{sw,Aln}$, which produced MAE, MRE, and RMSE values of 24.6 W m^{-2} ,
312 3.0%, and 32.2 W m^{-2} , respectively, and Pearson’s correlation coefficient of 0.941 (Fig. 3). The model
313 $R_{sw,Z.2}$ resulted in values of MAE, MRE, and RMSE close to those calculated for $R_{sw,Aln}$, that were
314 28.7 W m^{-2} , 3.4% and 33.8 W m^{-2} , and Pearson’s correlation coefficient of 0.939. Bisht et al. (2005);
315 Bisht et al. (2010); and Silva et al. (2015) also reported values for R_{sw} that were close to their
316 measured values by adopting $\beta = 0.2$, although the β value originally adopted by Zillman (1972) was
317 0.1. On average the $R_{sw,Aln}$ model showed an improvement of around 3% (referring to MRE)
318 compared to $R_{sw,Z.1}$ and less than 1% compared to $R_{sw,Z.2}$.

319 There is a large difference between the smallest value (Jun 10, 2017 – DOY 161) of $R_{sw,24}$ ($R_{sw,24}$
320 = 230.5 W m^{-2}) and the highest value (Dec 14, 2015 – DOY 348) of $R_{sw,24}$ ($R_{sw,24} = 350.3 \text{ W m}^{-2}$)
321 (Table S3), as a result of the seasonality of solar radiation associated to the differences in cloud cover,
322 and also to the transmittance data.

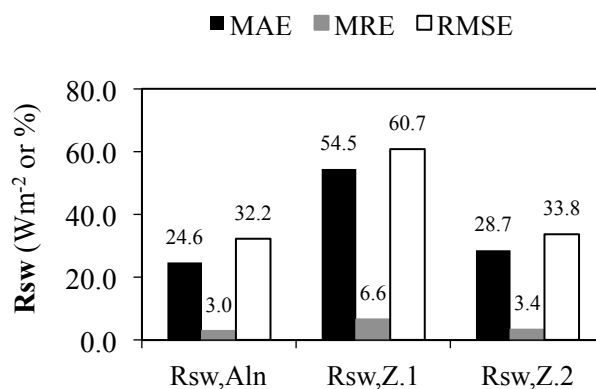


Figure 3. MAE (W m^{-2}), MRE (%), and RSME (W m^{-2}) related to the comparison between instantaneous *measured* R_{sw} and downwelling shortwave radiation obtained with models provided by Allen et al. (2007)— $R_{sw,Aln}$, and Zillman (1972)— $R_{sw,Z}$ with $\beta = 0.10$ and 0.20 , respectively.

323 3.2 Atmospheric longwave radiation

324 The observed values of atmospheric downwelling longwave radiation ($R_{lw,obs}$) and the estimated
 325 ones are in Table S4 in the supplementary material. The accuracy of the models, against
 326 measurements taken with an Eppley pyrgeometer, installed at the SONDA station, was tested with the
 327 statistical parameters MAE ($W m^{-2}$), MRE (%), and RMSE ($W m^{-2}$) (Fig. 4). The ϵ_a models that gave
 328 the best R_{lw} estimates were, in descending order of performance, those of Duarte et al. (2006),
 329 Bastiaanssen et al. (1998), Sugita and Brutsaert (1993), and Santos et al. (2011), which resulted in
 330 MAE values of $5.9 W m^{-2}$, $10.7 W m^{-2}$, $11.3 W m^{-2}$, and $11.7 W m^{-2}$; MRE values of 1.6%, 2.9%,
 331 3.1%, and 3.2%; and RMSE values of $7.0 W m^{-2}$, $13.0 W m^{-2}$, $12.5 W m^{-2}$, and $12.8 W m^{-2}$,
 332 respectively.

333 Based on the mean errors results we selected the model proposed by Duarte et al. (2006)
 334 (referred to as the Duarte model); it showed a relative improvement in estimated R_{lw} of around 8% in
 335 relation to the worst performing model (Idso and Jackson, 1969). Silva et al. (2015), who evaluated
 336 nine out of the ten models used in the present study at the Mogi Guaçu watershed (a subtropical
 337 Brazilian River basin), also concluded that the Duarte model provided the smallest RMSE ($7.4 W m^{-2}$)
 338 when compared to observed data.

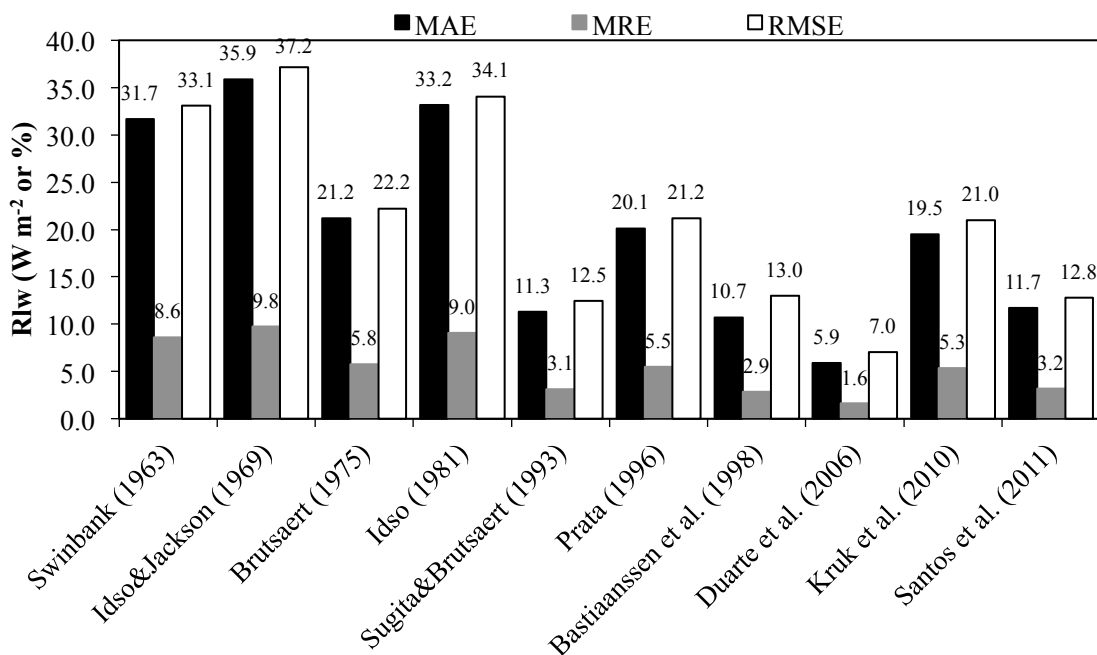


Figure 4. A comparison of the errors (MAE ($W m^{-2}$), MRE (%), and RMSE ($W m^{-2}$)) between

values of in-situ measured longwave downwelling radiation, and R_{lw} obtained with Stefan-Boltzmann's Law (Eq. 13), using ten different models of atmospheric emissivity; numbers at the top denote the actual percentages.

339

340 3.3 Overpass and daily net radiation

341 The MAE, MRE and RMSE for the comparison between in-situ measured R_n at the time of
 342 overpass and $R_{n,over}$ obtained with remote sensing (using Eq. 1, and related equations) were equal to
 343 38.8 W m^{-2} , 6.3% and 45.3 W m^{-2} for sugarcane; 60.8 W m^{-2} , 9.4% and 65.8 W m^{-2} for pristine
 344 caatinga and 84.6 W m^{-2} , 14% and 89.3 W m^{-2} for the mango orchard, respectively. Therefore, the
 345 estimated instantaneous values of R_n were very satisfactory for SC and PC, but not so much for MO.

346 The accuracy of $R_{n,24}$ modeled with Eq. 14 and Eq. 15 was compared to the daily R_n values
 347 measured onsite, using MAE, MRE, and RMSE (Table 2). The results indicate that the values
 348 obtained with the original model of Bisht et al. (2005), that is, $R_{n,24,Bst}$, produced very high errors. The
 349 reason for these high errors is that the Bisht model disregards the negative values that occur during the
 350 night period and part of the daytime period. This method considers the daily value to be the R_n value
 351 integrated over the instances for which $R_n > 0$, and divides it by the interval of time corresponding to
 352 that period. Instead, when we divide the integrated value for the time period during which $R_n > 0$, by
 353 the time corresponding to the entire daily period (86400 seconds), referred to as Bisht's corrected
 354 method, the error indicator values decrease considerably, although they are still relatively large. In
 355 contrast, when using the $R_{n,24,DeB}$ model, in the same way as proposed in the Surface Energy Balance
 356 Algorithm for Land – SEBAL (Bastiaanssen et al., 2000), the results were very satisfactory, even for
 357 the mango orchard, with MRE reduced from 14% (at the overpass) to 9.3% (24 hours).

358

359 **Table 2.** MAE (W m^{-2}), MRE (%), and RMSE (W m^{-2}) of R_n estimated by Eq 14 – $R_{n,24,DeB}$ and
 360 Eq. 15 – $R_{n,24,Bst}$ compared with at the sugarcane field (SC), pristine caatinga (PC) and mango orchard
 361 (MO)

| | Bisht method | | | Bisht's method corrected | | | De Bruin method | | |
|------------|------------------|------------------|------------------|--------------------------|------------------|------------------|------------------|------------------|------------------|
| | $R_{n,24}$ SC | $R_{n,24}$ PC | $R_{n,24}$ MO | $R_{n,24}$ SC | $R_{n,24}$ PC | $R_{n,24}$ MO | $R_{n,24}$ SC | $R_{n,24}$ PC | $R_{n,24}$ MO |
| MAE | 316.2 | 288.8 | 252.9 | 44.6 | 23.9 | 22.7 | 8.2 | 9.7 | 14.5 |
| MRE | 193.5 | 161.1 | 160.4 | 28.0 | 14.2 | 15.0 | 4.9 | 5.5 | 9.3 |

RMSE 317.6 290.2 253.7 46.4 25.8 24.6 9.3 12.6 16.4

362

363 In a different climatic region, Silva et al. (2015) obtained MAE, MRE, and RMSE values equal
364 to 8.3 W m^{-2} , 8.4%, and 10.4 W m^{-2} , respectively, for a sugarcane plantation, and 6.5 W m^{-2} , 6.3%,
365 and 8.5 W m^{-2} , respectively, in a Cerrado forest formation, using $R_{n,24,DeB}$ model. The RMSE values
366 obtained by Bisht et al. (2005) (Southern Great Plains, in USA), Ryu et al. (2008) (flat farmland site
367 and rugged forest in South Korea), Wang and Liang (2009) (grassland, cropland, and desert land
368 cover, in USA), Bisht and Bras (2010) (Southern Great Plains, in USA), and Jin et al. (2011)
369 (deciduous broadleaf forest, mixed forest, evergreen needleleaf forest and Shrubland, in USA) were
370 all higher than those obtained in the present study.

371 It is important to consider that the in-situ net radiometer instrument has an accuracy of 2.5% for
372 instantaneous measurements (note that we use averages that were recorded at 30-minute intervals for
373 SC and PC towers, and at 10-minute intervals in MO tower), increasing to 10% for daily
374 measurements (Silva et al., 2015). The same authors considered that, depending on the height of the
375 in-situ radiometer, the spatial resolution of TM and OLI/TIRS images is compatible with the coverage
376 area of the measurements performed with a 4-component radiometer. The radiometer installed on the
377 micrometeorological towers were 6, 8 and 14 meters above the ground for MO, SC and PC which
378 corresponds to a field of view of 11304, 20096 and 61544 m^2 respectively (considering a field of
379 vision of 180°). Hence, it is appropriate to compare measurements of in-situ R_n against estimates by
380 remote sensing (with resolution of 30–100 m, i.e. areas of 900 to 10,000 m^2 per pixel).

381 In Fig. 5, we show the values of the daily net radiation *measured* at the SC, PC and MO ($R_{n,24,obs}$)
382 pixels versus the values obtained by Eq. 14 ($R_{n,24,DeB}$) and Eq. 15, corrected as explained above,
383 ($R_{n,24,Bst}$). It is clear that there is greater agreement between the measured data and those of $R_{n,24,DeB}$,
384 which resulted in a greater Pearson correlation coefficient (r) and smaller Coefficient of Residual
385 Mass (CRM), with r ranging from 0.881 to 0.943, and CRM between 0.008 and 0.083. The
386 correlation between the measurements of $R_{n,24}$ with those obtained according to $R_{n,24,Bst}$ were lower
387 than those found for $R_{n,24,DeB}$ for SC, comparable for MO and higher for PC, nevertheless.

388 Nevertheless, the CRM (ranging from 0.132 to 0.271) indicates that $R_{n,24,Bst}$ overestimates the
 389 measured data considerably, for the studied surfaces.

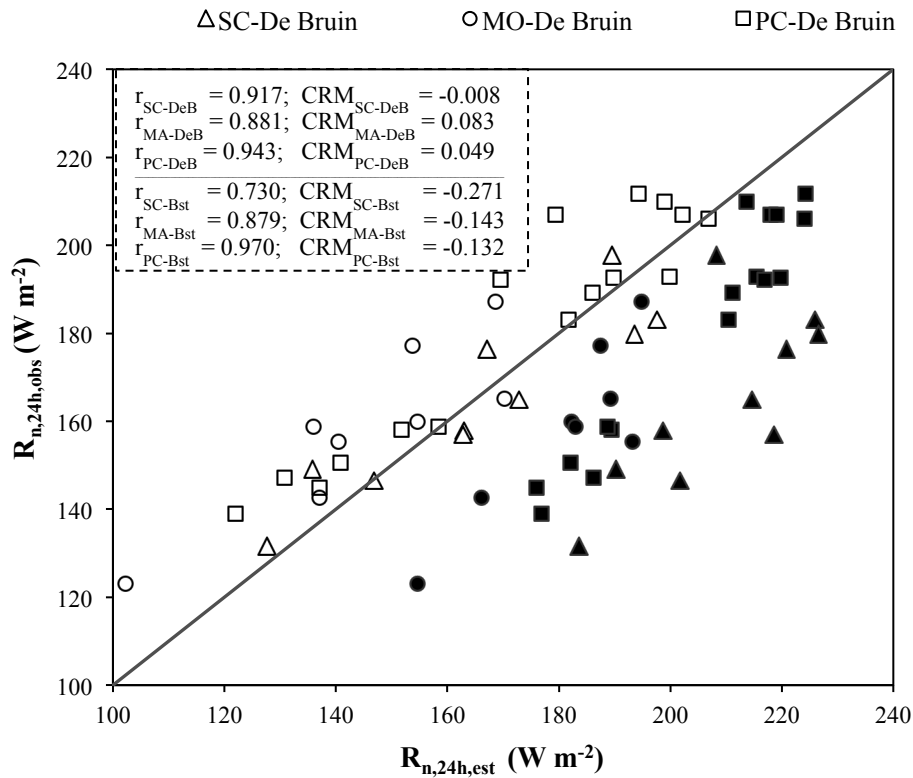


Figure 5. Representation of $R_{n,24,est}$ ($R_{n,24}$ estimated, $W m^{-2}$) by Eq. 14 – $R_{n,24,DeB}$ and Eq. 15 – $R_{n,24,Bst}$ compared with integrated observed values of net radiation for the three vegetated surfaces: sugarcane (SC), mango orchard (MO) and pristine caatinga (PC) - $R_{n,24,obs}$

390 The data of $R_{n,24,Bst}$ overestimate $R_{n,24,obs}$ by disregarding the negative values of R_n , occurring
 391 throughout the night and for almost an hour after sunrise and before sunset. It is very important to
 392 note that in applications where $R_{n,24}$ is required to determine the evapotranspiration by remote sensing,
 393 it would be advisable not to use the Bisht method, since it overestimates the $R_{n,24}$ by more than 100%.
 394 However, despite the poor performance of the sinusoidal model (Eq. 15) on a daily basis, it presents
 395 good agreement with instantaneous $R_n(t)$ values when R_n is positive (Fig. 6).
 396
 397

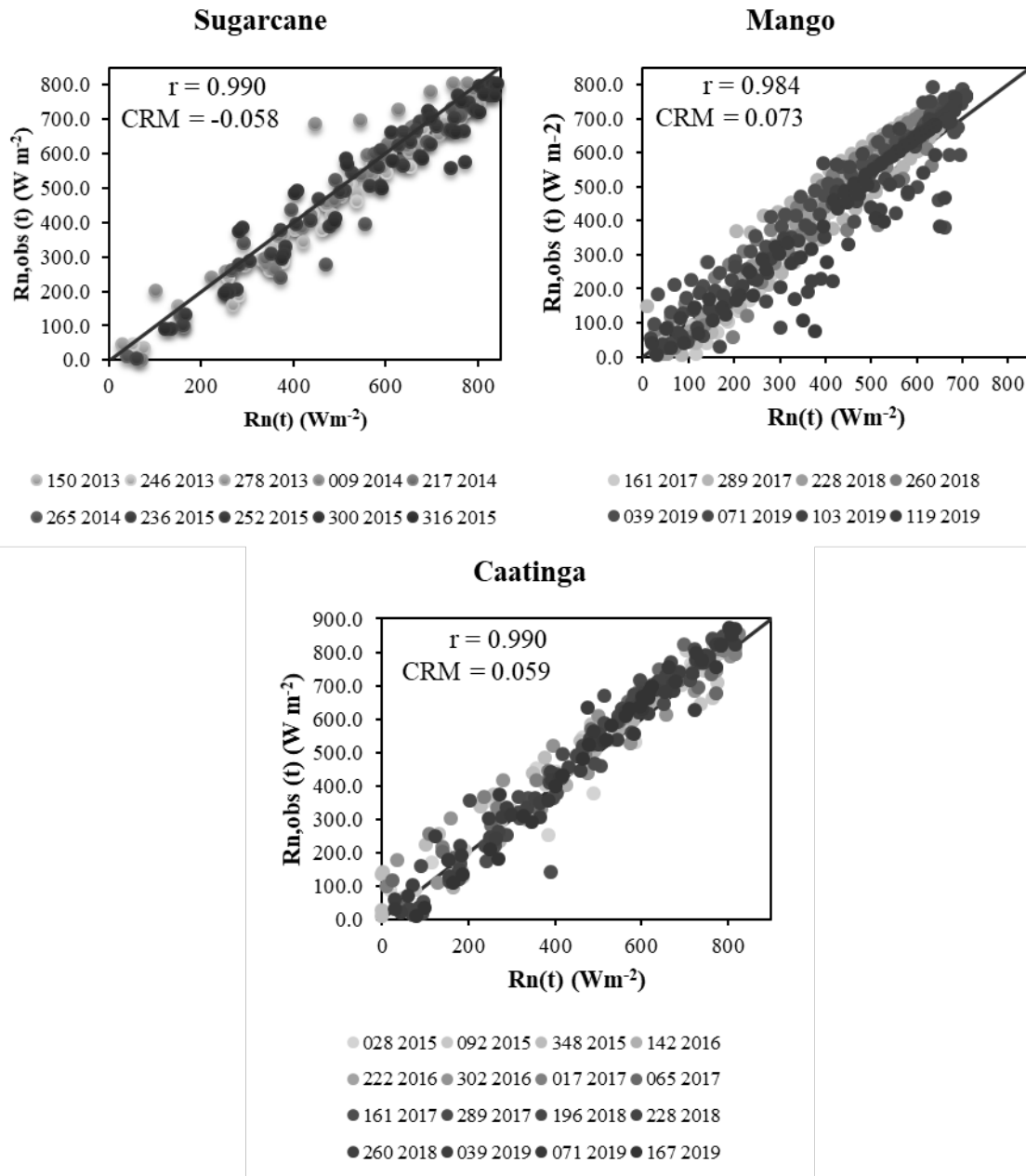


Figure 6. Performance of sinusoidal model for $R_n(t)$ (Eq. 2) as compared with $R_{n,obs}(t)$ over a sugarcane field (SC), mango orchard (MO) and pristine caatinga (PC). The legend indicates the day number and year of points on the plots (for each day the values were computed at the same interval as the measurements were conducted at the micrometeorological towers – 10 minutes for the MO and 30 minutes for SC and PC).

399 Land use change, as a result of the replacement of primary vegetation by grassland, agricultural
400 crops, and urban occupation, can substantially affect the exchange of heat and mass in the soil-plant-
401 atmosphere system. Fig. 7 shows the spatial distribution of albedo, NDVI, land surface temperature—
402 LST (°C), and surface emissivity— ϵ_0 obtained from remote sensing on January 9, 2014. In these maps
403 there is an obvious presence of the São Francisco riverbed crossing the study area from west to
404 northeast; it stands out due to low albedo values (water bodies generally have values of 0.05-0.08) and
405 low LST values (< 20 °C, much lower than the air temperature). Irrigated and urban areas show
406 considerably different pixel values and patterns of NDVI, LST, and ϵ_0 .

407 The urban areas of the municipality of Petrolina and Juazeiro cities have high albedo values,
408 which means greater reflection of downwelling shortwave radiation, and the LST is high, which
409 increases the emitted longwave radiation. Consequently, the instantaneous net radiation over urban
410 areas (as calculated using Eq. 1) is smaller than that over the vegetated surfaces, especially the
411 irrigated plots, where albedo and LST are much lower.

412 Selected images, as shown in Fig. 8, presented $R_{n,over}$ ($W m^{-2}$) for: a) January 9, 2014 – DOY 9;
413 b) September 22, 2014 – DOY 265; c) August 24, 2015 – DOY 236; and November 12, 2015 – DOY
414 316. The values of $R_{n,over}$ obtained over the entire study area are highest for January 9, 2014 (Fig. 7-d
415 and 9-a), ranging from $260.8 W m^{-2}$ to $722.0 W m^{-2}$. On August 24, 2015 (Fig. 8-c) the values are the
416 lowest, although the patterns are basically the same as those shown in the other maps, as a
417 consequence of the lower downwelling shortwave radiation— R_{sw} on this day, caused by low τ_{sw}
418 (related to atmospheric conditions), dr (due to higher earth-sun distance) and $\cos(Z)$ (due to
419 seasonality), (see Tables S2 and S3).

420 For reasons explained previously the river exhibits the highest values of $R_{n,over}$, followed by the
421 caatinga vegetation and the irrigated plots, particularly those located to the southeast of the São
422 Francisco river. The net shortwave radiation for the caatinga vegetation is generally higher than in the
423 agricultural areas, due to its lower albedo; however, the longwave radiation emitted by caatinga is also
424 expected to be higher (higher LST). The caatinga often presents low LAI (except in the wet season)
425 (Miranda et al., 2020), which means a lower emissivity (Fig. 7d), due to the fact that the emissivity of
426 soil is generally lower than that of leaves; therefore, despite the fact that the Caatinga has high values

427 of LST⁴, it has a lower emissivity than the irrigated areas. This combination makes the caatinga R_n
428 similar to that of agricultural land during large parts of the year (Carvalho et al., 2018a).

429 Although R_n of the irrigated areas is similar to that of the caatinga areas, the irrigated areas use a
430 large part of this energy for transpiration (Carvalho et al., 2018; Teixeira et al., 2008), as it has higher
431 soil moisture contents, which leads to a lower LST which may impact the local climate over these
432 areas. It is very likely that these crops are using energy advected from nearby drier areas (e.g. pasture
433 or thin caatinga with exposed soil, with much higher sensible heat fluxes) (Oliveira & Leitao, 2000),
434 causing the surface temperatures of the irrigated areas to decrease even more.

435 It can be observed that in the areas dominated by pasture and urban infrastructure, the values of
436 LST and albedo are higher, and NDVI and $R_{n,over}$ are lower, than those calculated for caatinga and
437 crops. For pasture, this may be due to lower plant density, which results in more dry exposed soil,
438 with higher albedos and lower rates of cooling evaporative fluxes, which will increase LST. Another,
439 related, factor contributing to high rangeland LSTs is the fact that grasses have shallow roots and can,
440 therefore only access near-surface soil moisture, which is more rapidly depleted.

441 Bezerra et al. (2013) showed that rural areas presented air temperatures that were lower
442 (difference on the air minimum temperature recorded of 5.9 °C and for the air maximum temperature
443 of 2.3 °C) than the temperature measured for the city of Petrolina. It is a fact that the caatinga
444 vegetation can present various physiognomies (from woodlands to sparsely distributed thorny shrubs;
445 Silva et al., 2017), and each of these has a different vegetation structure. The grazing that occurs at
446 some Caatinga sites also impacts the vegetation density, and consequently its spatiotemporal
447 dynamics, and related surface variables such as NDVI (Silveira et al., 2018), LST, albedo and
448 emissivity. Ultimately, this will affect the micro- and regional climate and soil-land-surface-
449 atmosphere fluxes.

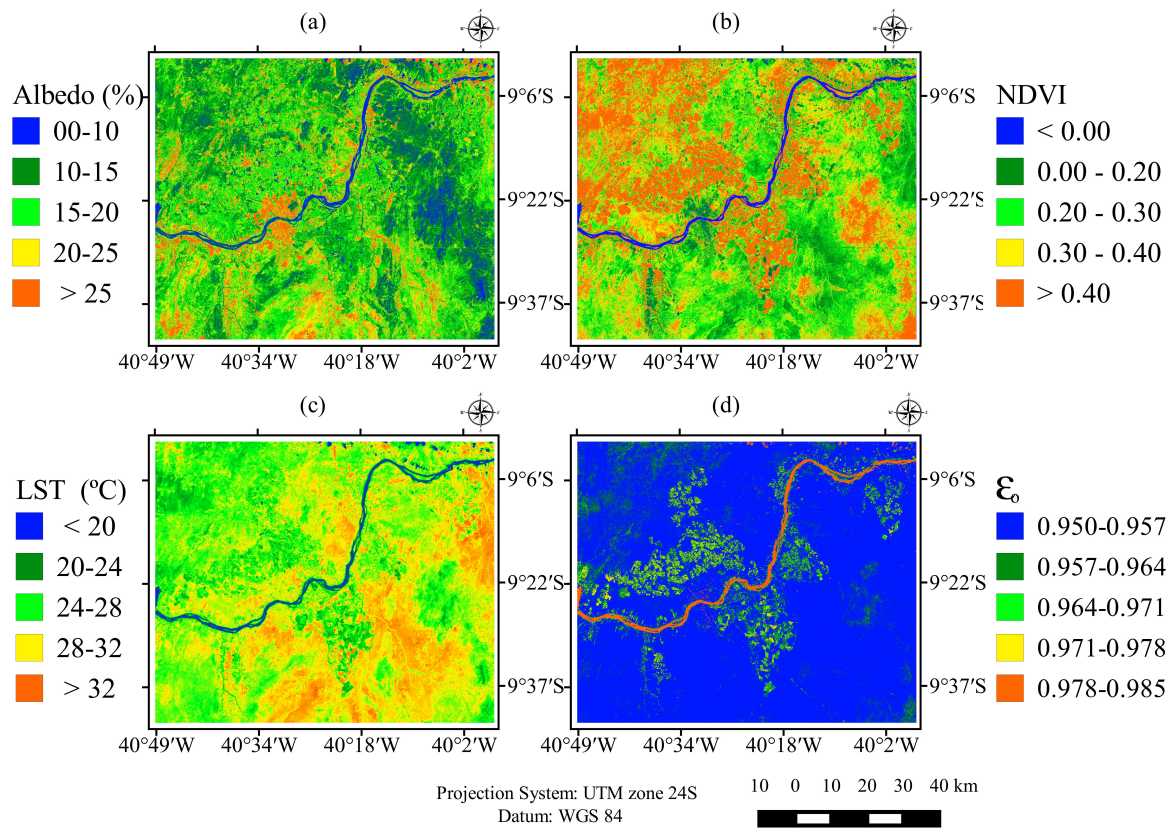


Figure 7. (a) Instantaneous albedo, (b) NDVI, (c) LST, and (d) ϵ_0 on January 9, 2014 – DOY 9.

450

451 In an oasis area, Bastiaanssen et al. (1998) reported $R_{n,over}$ values close to 600 W m^{-2} and smaller
 452 than 400 W m^{-2} for desert pixels in summer. At the Mogi-Guaçu watershed in southeast Brazil, a
 453 semi-humid region, Silva et al. (2015) recorded R_n values, during 2005, similar to those observed in
 454 this study over urban and agricultural areas, despite the fact that climatic conditions were different.
 455 Bare soil R_n values ranging between $310\text{--}430 \text{ W m}^{-2}$ (between spring and summer) were detected in a
 456 semi-arid area of Brazil (Di Pace et al., 2008) and between $500\text{--}550 \text{ W m}^{-2}$ (in summer) in a region
 457 with high advective effects (Chavez et al., 2007). However, it is important to consider that values of
 458 R_n depend on the complex interactions within the soil-plant-atmosphere system, and on the local
 459 seasonal evolution and patterns of rainfall and downwelling radiation components, as well as on the
 460 highly dynamic nature of the crop management and irrigated agricultural activities taking place in this
 461 important area of agricultural production.

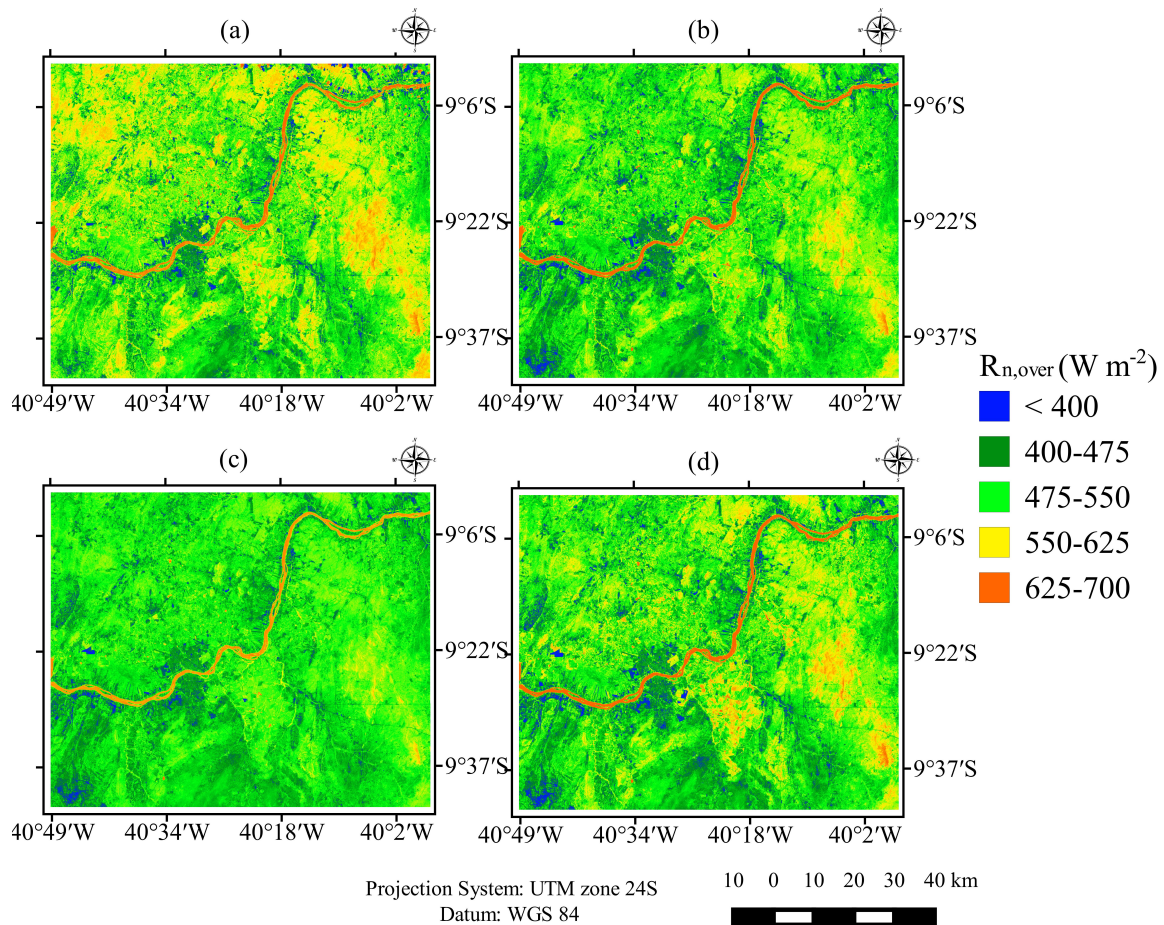


Figure 8. Instantaneous net radiation during satellite overpass— $R_{n,over}$ ($W m^{-2}$) as calculated from remote sensing information on: a) January 9, 2014; b) September 22, 2014; c) August 24, 2015 and d) November 12.

462

463 3.5 Estimates of daily net radiation

464 In Fig. 9, maps of $R_{n,24,DeB}$ values for June 2, 2014 (DOY = 153) and November 12, 2015 (DOY =
 465 316) are shown. The $R_{n,24,DeB}$ patterns are similar to those obtained for $R_{n,over}$ (see Fig. 8). The
 466 seasonality of R_n can be observed in this figure; in June most of the $R_{n,24,DeB}$ values were between 60
 467 and $160 W m^{-2}$ (close to the winter solstice, with $R_{sw,24}$ of $245.1 W m^{-2}$ and $\tau_{sw,24}$ of 0.709, see Table
 468 S3), whereas a substantial increase in R_n was found for November, resulting in values between 80 and
 469 $200 W m^{-2}$ (close to the summer solstice, with $R_{sw,24}$ of $326.7 W m^{-2}$ and $\tau_{sw,24}$ of 0.721, see Table S3).
 470 Silva et al. (2011), for a semiarid region, found $R_{n,24,DeB}$ values between 146.8 (September 14, 2008)

471 and 164.7 (December 19, 2008) $W m^{-2}$ for an irrigated banana orchard, and between 95.6 and 112.5
472 m^{-2} (on the same dates) for bare soil.

473

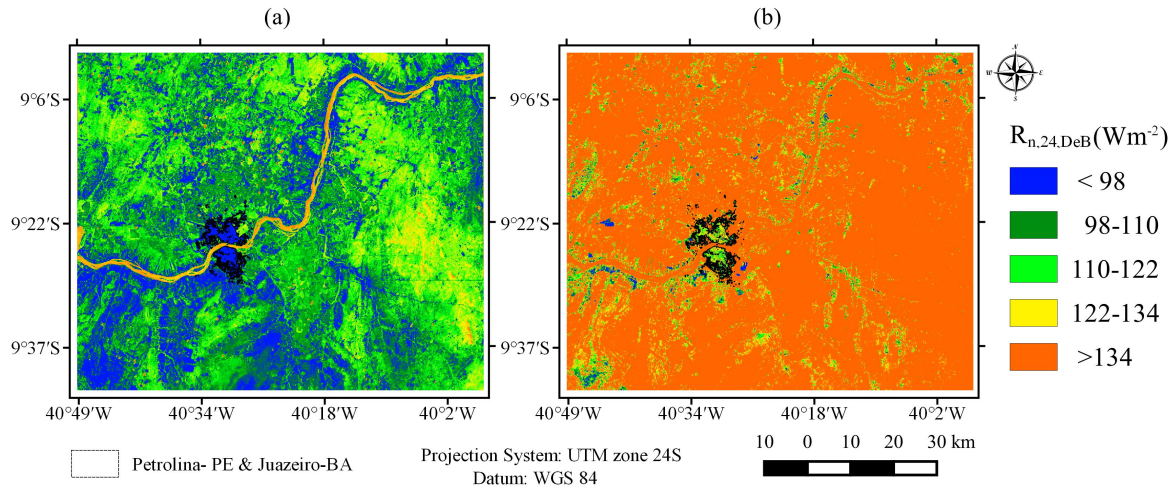


Figure 9. Daily net radiation— $R_{n,24,DeB}$ ($W m^{-2}$) on: a) June 2, 2014 (DOY 153) and b) November 12, 2015 (DOY 316).

474

475 3.6 The effect of land use changes on net radiation

476 Fig. 10 presents the box-plot diagrams for the same variables as presented in Fig. 7, NDVI, LST
477 (K), albedo, surface emissivity, ϵ_0 , and for $R_{n,over}$ ($W m^{-2}$), generated from the pixel data for the four
478 contrasting land-cover types (100 random points extracted for each land-cover type, see Section 2.1).
479 The irrigated pixels have a higher NDVI and ϵ_0 and lower LST than the other types, while $R_{n,over}$ is
480 similar and albedo is slightly higher than the values found for caatinga (as mentioned above). The
481 variability (as indicated by the interquartile range) of NDVI, ϵ_0 and LST of irrigated areas is much
482 higher than that calculated for other areas, indicating that the existence of different crops and their
483 different cultivation phases, result in greater spatiotemporal variability than the variability caused by
484 seasonality for pasture and Caatinga.

485 Figure 10 shows that the highest R_n values were mostly found for irrigated agriculture and the
486 caatinga. We would expect high values for the irrigated agriculture, because their low LST values and
487 low albedo values result in large values of net longwave and net shortwave radiation. However, high

488 R_n values are not so obvious for the caatinga because it has high surface temperatures, hence in
489 principle should have high longwave upwelling radiation. However, its relatively low value of surface
490 emissivity, ϵ_0 , tempers the losses resulting from longwave upwelling radiation to a certain degree.
491 Note also, that the albedo values for caatinga are the lowest among all land cover types (including
492 crops), which results in larger values of net shortwave for this surface cover. Pasture has the lowest R_n
493 values among the vegetated land cover types. This is caused by the fact that its LSTs are even higher
494 than those for caatinga and its ϵ_0 is comparable to that of caatinga so that its net longwave radiation is
495 the lowest (i.e. more negative than for the other surface types). At the same time, the albedo for
496 pasture is considerably larger than that of caatinga, causing net shortwave radiation also to be low for
497 pasture. Interestingly, the LST values for urban areas are comparable to those of caatinga and pasture,
498 in some cases they are even lower; also, urban emissivities are comparable or lower than those of
499 caatinga and pasture, so that urban net longwave radiation is higher or comparable to that of caatinga
500 and pasture. Yet, their R_n values are the lowest of all surface types, because of their high albedo.

501 In summary, if pristine caatinga (PC) is turned to rangeland then albedo will increase, LST will
502 be slightly higher and R_n lower. If it is changed to urban areas, albedo will increase, but LST will in
503 fact be similar or slightly lower, and R_n will be lower. If it is turned to irrigated crops, albedo will be
504 slightly higher, LST 3-5 degrees lower, yet R_n will remain similar to the values calculated for PC, as a
505 result of the considerably lower surface emissivity for caatinga. Fig. S1 (in the supplementary
506 material) illustrates the impact on the net radiation, discussed above, caused by land use change over
507 the study period, for two subsets of the study area.

508 These data illustrate that land use substantially affects net radiation, via its upwelling shortwave
509 and longwave components. This will affect the available energy (net radiation minus storage of heat
510 in the vegetation and soil) and possibly aerodynamic roughness parameters (e.g. crops will have a
511 lower roughness length and displacement height), which will affect the exchange of water vapour and
512 heat between the land surface and the atmosphere (data not shown). These combined effects will have
513 an impact on the climate locally, via land-surface atmosphere feedbacks, if the size of the changed
514 area is relatively large and fairly homogeneous, as in the case for caatinga in this study.

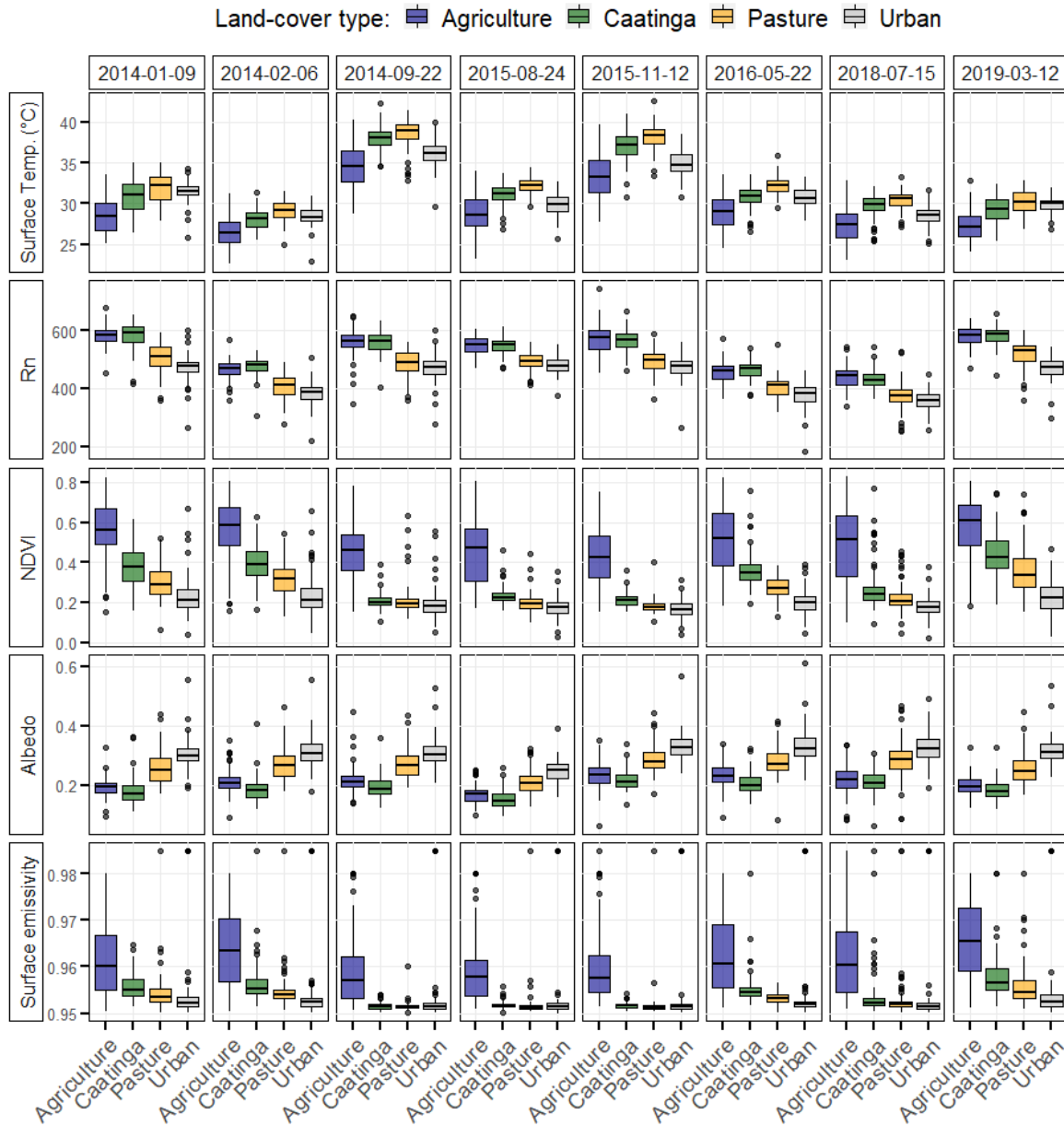


Figure 10. Box-plot diagrams of the LST (K), $R_{n,over}$ ($W m^{-2}$), NDVI, , Albedo and surface emissivity for agriculture (irrigated), urban infrastructure, caatinga vegetation and pasture.

515

516 **4. Conclusions**

517

518 The effects that climate and seasonality have on the downwelling components and that land use
 519 has on the upwelling components of the surface radiation balance were evaluated for a semiarid area
 520 in Brazil (within the Brazilian Caatinga), consisting of a mosaic of remaining areas of pristine natural

521 seasonally dry forest vegetation (caatinga), irrigated agriculture and semi-natural rangeland. We used
522 two models to calculate downwelling shortwave radiation, and ten models of clear-sky atmospheric
523 emissivity to calculate downwelling longwave radiation following the Stefan Boltzmann's equation.
524 We used Landsat 8 satellite images to derive the required biophysical variables, such as albedo and
525 land surface temperature, and climate variables measured at a nearby weather station were used to
526 calculate longwave downwelling radiation. The selected shortwave and longwave models performed
527 well when compared against in-situ SONDA station measurements as evaluated using the MAE,
528 MRE, and RMSE metrics.

529 The spatial patterns obtained show that the land-use, in particular the caatinga vegetation cover,
530 substantially affects those components of the net radiation that depend on the type and state of the
531 land surface cover, such as reflected shortwave radiation and emitted longwave radiation. It is
532 important that reliable equations are employed to calculate the separate components of net radiation,
533 so that subsequent estimates of sensible and latent heat flux are more accurate.

534 In this context, we show that the sinusoidal model (Bisht, 2005), used for determination of the
535 daily net radiation from instantaneous values of R_n determined from remote sensing, considerably
536 overestimates daily net radiation estimates, $R_{n,24}$, as a consequence of the fact that this model does not
537 consider the negative values of R_n that occur throughout the night period and part of the daytime
538 period. On the other hand, the De Bruin model, that only uses remote sensing-based values of net
539 shortwave radiation (and an empirical term, derived from weather data, to represent net longwave
540 radiation), performed very satisfactorily.

541 In the rangeland, the albedo, land surface temperature, LST, and hence the upwelling shortwave
542 and longwave radiation components, had greater values than in the pristine caatinga, which
543 contributes to a reduction in the net radiation at the surface, and most likely an increase in sensible
544 heat flux via higher LSTs (data not shown). In the urban areas, the LST and the surface emissivity are
545 comparable to those found for the caatinga and pasture values, but the albedo values are the highest of
546 all surface types, which resulted in the lowest net shortwave radiation and consequently, the lowest
547 R_n . The albedo in the irrigated agricultural crops is 0.01–0.03 greater than in the pristine caatinga, and

548 the LST is 3–5 degrees smaller; yet, R_n for these two land uses is similar, as a result of considerably
549 lower surface emissivity for caatinga.

550 We provide evidence that when in-situ data of net radiation are not available, remote sensing
551 data, combined with more readily available data such as air temperature, pressure and humidity, can
552 be used to derive reliable spatiotemporal estimates of R_n that can identify environmental and
553 anthropogenic, and short-term as well as long-term, impacts on the land surface radiation balance, and
554 ultimately on the energy balance. We would like to emphasize that remote sensing studies, such as the
555 one presented here, are crucial in the determination of the available energy for the turbulent fluxes
556 (e.g. evapotranspiration, ET) between the surface and the atmosphere, on the regional scale. Reliable
557 estimation of ET is of great importance in the context of irrigation planning and wider water
558 management, again underlining the need for reliable and accurate data.

559

560

561 **Funding:**

562 This research was partly supported by the National Council for Scientific and Technologic
563 Development - CNPq and Coordination for the Improvement of Higher Education Personnel - CAPES
564 of Brazil government. MSBM, AV and RLBN acknowledge support from the UK/Brazil Nordeste
565 project, funded jointly through the UK Natural Environment Research Council (NE/N012488/1 UoR
566 and NE/N012526/1 ICL) and FAPESP (São Paulo Research Foundation) (FAPESP 2015/50488-5),
567 and MSBM thank to Fundação de Amparo à Ciência e Tecnologia do Estado de Pernambuco for
568 funding this through the Project FACEPE APQ 0062-1.07/15 (Caatinga-FLUX).

569 **Declarations of interest:**

570 None.

571 **Appendix A. Supplementary data:**

572 Supplementary data to this article can be found online at...

573 **References**

574 Alados, I., Foyo-Moreno, I., Alados-Arboledas, L. (2012). Estimation of downwelling longwave
575 irradiance under all-sky conditions. *Int. J. Climatol.* 32 (5), 781–793.
576 <https://doi.org/10.1002/joc.2307>.

577 Allen, R. G. (1996). Assessing integrity of weather data for use in reference evapotranspiration
578 estimation. *J. Irrig. Drain. Eng.*, 122(2), 97–106. [https://doi.org/10.1061/\(ASCE\)0733-
579 9437\(1996\)122:2\(97\)](https://doi.org/10.1061/(ASCE)0733-9437(1996)122:2(97))

580 Allen, R., Irmak, A., Trezza, R., Hendrickx, J. M. H., Bastiaanssen, W., & Kjaersgaard, J. (2011).
581 Satellite-based ET estimation in agriculture using SEBAL and METRIC. *Hydrological
582 Processes*, 25, 4011–4027. <http://dx.doi.org/10.1002/hyp.8408>

583 Allen, R. G., Tasumi, M., Trezza, R. (2007). Satellite-based energy balance for mapping
584 evapotranspiration with internalized calibration (METRIC) - Model. *J. Irrig. Drain. Eng.*, 133,
585 380-394. [https://doi.org/10.1061/\(ASCE\)0733-9437\(2007\)133:4\(380\)](https://doi.org/10.1061/(ASCE)0733-9437(2007)133:4(380)).

586 ASCE–EWRI. (2005). The ASCE standardized reference evapotranspiration equation. ASCE–EWRI
587 Standardization of Reference Evapotranspiration Task Committee Rep., ASCE Reston, Va.
588 [https://doi.org/10.1061/40499\(2000\)126](https://doi.org/10.1061/40499(2000)126)

589

590 Bastiaanssen, W. G. M. (2000). SEBAL-based sensible and latent heat fluxes in the irrigated Gediz
591 Basin, Turkey. *J. Hydrol.*, 229, 87–100. [https://doi.org/10.1016/S0022-1694\(99\)00202-4](https://doi.org/10.1016/S0022-1694(99)00202-4).

592 Bastiaanssen, W. G. M., Menenti, M., Feddes, R. A., Holtslag, A. A. M. (1998). A remote sensing
593 surface energy balance algorithm for land (SEBAL). 1: Formulation. *J. Hydrol.*, 212–213, 98–
594 212. [https://doi.org/10.1016/S0022-1694\(98\)00253-4](https://doi.org/10.1016/S0022-1694(98)00253-4).

595 Bastiaanssen, W. G. M., Noordman, E. J. M., Pelgrum, H., Davids, G., Thoreson, B. P., Allen, R.G.
596 (2005). SEBAL model with remotely sensed data to improve water resources management
597 under actual field conditions. *J. Irrig. Drain. Eng.*, 131(1), 85–93.
598 [https://doi.org/10.1061/\(ASCE\)0733-9437\(2005\)131:1\(85\)](https://doi.org/10.1061/(ASCE)0733-9437(2005)131:1(85)).

599 Bezerra, P. T. C., Leitão, M. M. V. B. R., Azevedo, P. V. (2013). Ilhas de Calor e Desconforto
600 Térmico no Semiárido Brasileiro: Um Estudo de Caso na cidade de Petrolina-PE. *Rev. Bras.*
601 *Geogr. Fís.*, 6, 427-441.

602 Bisht, G., Bras, R. L. (2010). Estimation of net radiation from the MODIS data under all sky
603 conditions: Southern Great Plains case study. *Remote Sens. Environ.*, 114, 1522-1534.
604 <https://doi.org/10.1016/j.rse.2010.02.007>.

605 Bisht, G., Bras, R. L. (2011). Estimation of net radiation from the Moderate Resolution Imaging
606 Spectroradiometer over the continental United States. *IEEE Trans. Geosci. Remote Sens.*, 49,
607 2448–2462. <http://dx.doi.org/10.1109/TGRS.2010.2096227>.

608 Bisht, G., Venturini, V., Islam, S., Jiang, L. (2005). Estimation of the net radiation using MODIS
609 (Moderate Resolution Imaging Spectroradiometer) data for clear-sky days. *Remote Sens.*
610 *Environ.*, 97, 52–67. <https://doi.org/10.1016/j.rse.2005.03.014>.

611 Brutsaert, W. (1975). On a derivable formula for long-wave radiation from clear skies. *Water Resour.*
612 *Res.*, 11, 742-744. <https://doi.org/10.1029/WR011i005p00742>.

613 Carvalho, H. F. S., Moura, M. S. B., Silva, T.G.F. (2018). Fluxos de radiação e energia em caatinga
614 preservada e cana-de-açúcar no Semiárido. *Rev. Bras. Meteorol.*, 33, 452-458.
615 <http://dx.doi.org/10.1590/0102-7786333005>.

616 Carmona, F., Rivas, R., & Caselles, V. (2014). Estimation of daytime downwelling longwave
617 radiation under clear and cloudy skies conditions over a sub-humid region. *Theoretical and*
618 *Applied Climatology*, 115, 281–295. <http://dx.doi.org/10.1007/s00704-013-0891-3>.

619 Chavez, J. L., Gowda, P. H., Howell, T. A., Marek, T. H. and New, L. L. (2007). Evapotranspiration
620 mapping using METRICTM for a region with highly advective conditions. In 2007 ASABE
621 Annual International Meeting, Technical Papers. Vol. 4. <https://doi.org/10.13031/2013.23414>.

622 Choi, M. (2013). Parameterizing daytime downwelling longwave radiation in two Korean regional
623 flux monitoring network sites. *J. Hydrol.* 476, 257–264.
624 <https://doi.org/10.1016/j.jhydrol.2012.10.041>

625 CNUC/MMA. Unidades de Conservação por Bioma. Available at
626 <http://www.mma.gov.br/images/arquivo/80238/CNUC_FEV18%20-%20C_Bio.pdf>. (last
627 accessed on 24 Apr 2018).

628

629 Cunha, J., Nóbrega, R., Rufino, I., Erasmi, S., Galvão, C., Valente, F. (2020). Surface albedo as a
630 proxy for land-cover clearing in seasonally dry forests: evidence from the Brazilian Caatinga.
631 *Remote Sens. Environ.* <https://doi.org/10.1016/j.rse.2019.111250>.

632 Driemel, A., Augustine, J., Behrens, K., Colle, S., Cox, C., Cuevas-Agulló, E., Denn, F. M., Duprat,
633 T., Fukuda, M., Grobe, H., Haeffelin, M., Hodges, G., Hyett, N., Ijima, O., Kallis, A., Knap,
634 W., Kustov, V., Long, C. N., Longenecker, D., Lupi, A., Maturilli, M., Mimouni, M.,
635 Ntsangwane, L., Ogihara, H., Olano, X., Olefs, M., Omori, M., Passamani, L., Pereira, E. B.,
636 Schmithüsen, H., Schumacher, S., Sieger, R., Tamlyn, J., Vogt, R., Vuilleumier, L., Xia, X.,
637 Ohmura, A., and König-Langlo, G. (2018). Baseline Surface Radiation Network (BSRN):
638 structure and data description (1992–2017), *Earth Syst. Sci. Data*, 10, 1491-1501,
639 <https://doi.org/10.5194/essd-10-1491-2018>.

640 De Bruin, H. A. R. (1987). From Penman to Makkink. In: Hooghart, J. C. (Ed.), *Proceedings and*
641 *information: TNO Committee on Hydrological*. Gravenhage, The Netherlands. 39, 5-31.

642 Di Pace, F. T., Silva, B. B. da, Silva, V. P. R., Silva, S. T. A. (2008). Mapeamento do saldo de
643 radiação com imagens Landsat 5 e modelo de elevação digital. *Rev. Bras. Eng. Agríc.*
644 *Ambient.*, 12, 385-392. <http://dx.doi.org/10.1590/S1415-43662008000400009>.

645 Duarte, H. F., Dias, N. L., Maggiotto, S. R. (2006). Assessing daytime downwelling longwave
646 radiation estimates for clear and cloudy skies in Southern Brazil. *Agric. For. Meteorol.*, 139,
647 171–181. <https://doi.org/10.1016/j.agrformet.2006.06.008>.

648 Elnmer, A., Khadr, M., Kanae, S., & Tawfik, A. (2019). Mapping daily and seasonally
649 evapotranspiration using remote sensing techniques over the Nile delta. *Agric. Water Manage.*,
650 213, 682-692.

651 Garrison, J.D., Adler, G.P. (1990). Estimation of precipitable water over the United States for
652 application to the division of solar radiation into its direct and diffuse components. *Sol. Energy*
653 44, 225–241. [https://doi.org/10.1016/0038-092X\(90\)90151-2](https://doi.org/10.1016/0038-092X(90)90151-2).

654 Hoagland, S.J., Beier, P., Lee, D. (2018). Using MODIS NDVI phenoclasses and phenoclusters to
655 characterize wildlife habitat: Mexican spotted owl as a case study. *For. Ecol. Manage.* 412, 80–
656 93. <https://doi.org/10.1016/j.foreco.2017.12.017>.

657 IBGE. Estados: População, Instituto Brasileiro de Geografia, Rio de Janeiro:
658 <<http://censo2010.ibge.gov.br/apps/atlas/>> (last accessed on July 2018).

659 Idso, S. B. (1981). A set of equations for full spectrum and 8 to 14 μm and 10.5 to 12.5 μm thermal
660 radiation from cloudless skies. *Water Resour. Res.*, 17, 295–304.
661 <https://doi.org/10.1029/WR017i002p00295>.

662 Idso, S. B., Jackson, R. D. (1969). Thermal radiation from the atmosphere. *J. Geophys. Res.*, 74, 5397–
663 5403. <https://doi.org/10.1029/JC074i023p05397>.

664 INMET. Instituto Nacional de Meteorologia. NORMAIS CLIMATOLÓGICAS DO BRASIL.
665 Available at <<http://www.inmet.gov.br/portal/index.php?r=clima/normaisclimatologicas>> (last
666 accessed on 30 Sep 2018).

667 Jensen, M. E., Allen, R. G. (2016). Evaporation, Evapotranspiration, and Irrigation Water
668 Requirements, ASCE Manuals and Reports on Engineering Practice No. 70. 2nd ed. American
669 Society of Civil Engineers, Reston, VA.

- 670 Jin, Y., Randerson, J. T., Goulden, M. L. (2011). Continental-scale net radiation and
671 evapotranspiration estimated using MODIS satellite observations. *Remote Sens. Environ.*, 115,
672 2302-2319. <https://doi.org/10.1016/j.rse.2011.04.031>.
- 673 Kilic, A., Allen, R., Trezza, R., Ratcliffe, I., Kamble, B., Robison, C., Ozturk, D. (2016). Sensitivity
674 of evapotranspiration retrievals from the METRIC processing algorithm to improved
675 radiometric resolution of Landsat 8 thermal data and to calibration bias in Landsat 7 and 8
676 surface temperature. *Remote Sens. Environ.*, 185, 198–209.
677 <https://doi.org/10.1016/j.rse.2016.07.011>.
- 678 Kruk, N. S., Vendrame, I. F., Rocha, H. R., Chou, S. C., Cabral, O. (2010). Downwelling longwave
679 radiation estimates for clear and all-sky conditions in the Sertãozinho region of São Paulo,
680 Brazil. *Theor. Appl. Climatol.*, 99, 115–123. <http://dx.doi.org/10.1007/s00704-010-0347-y>.
- 681 Kvalevag, M. M., Myhre, G., Bonan, G., Levis, S. (2010). Anthropogenic landcover changes in a
682 GCM with surface albedo changes based on MODIS data. *Int. J. Climatol.*, 30, 2105–2117.
683 <https://doi.org/10.1002/joc.2012>.
- 684 Li, Z., Wang, Z., Liu, X., Fath, B. D., Liu, X., Xu, Y., Hutjes, R., Kroeze, C. (2019). Causal
685 relationship in the interaction between land cover change and underlying surface climate in the
686 grassland ecosystems in China. *Sci. Total Environ.*, 647, 1080–1087.
687 [doi:10.1016/j.scitotenv.2018.07.401](https://doi.org/10.1016/j.scitotenv.2018.07.401).
- 688 Lin, J., Liu, X., Li, K., Li, X. (2014). A maximum entropy method to extract urban land by combining
689 MODIS reflectance, MODIS NDVI, and DMSP-OLS data. *Int. J. Remote Sens.* 35, 6708–6727.
690 <https://doi.org/10.1080/01431161.2014.960623>.
- 691 Liu, Z., Liu, Y., Baig, M. H. A. (2019). Biophysical effect of conversion from croplands to grasslands
692 in water-limited temperate regions of China. *Sci. Total Environ.*, 648, 315-324.
693 <https://doi.org/10.1016/j.scitotenv.2018.08.128>

694 Markham, B. L., Barker, J. L. (1986). Landsat MSS and TM post-calibration dynamic ranges,
695 exoatmospheric reflectances and at satellite temperatures. EOSAT Landsat Technical Notes
696 1:3-8, Earth Observation Satellite Company, Lanham, Md.

697 Marques, T. V., Mendes, K., Mutti, P., Medeiros, S., Silva, L., Perez-Marin, A. M., Campos, S.,
698 Lúcio, P. S., Lima, K., Reis, J., Ramos, T. M., Silva, D. F., Oliveira, C. P., Costa, G. B.,
699 Antonino, A. C. D., Menezes, R. S. C., Silva, C. M. S., Bezerra, B. G. (2020). Environmental
700 and biophysical controls of evapotranspiration from Seasonally Dry Tropical Forests (Caatinga)
701 in the Brazilian Semiarid. *Agric. For. Meteorol.* 287, 107957.
702 <https://doi.org/10.1016/j.agrformet.2020.107957>.

703 Melo, E.C., Correia, M.F., Aragão, M.S. (2015). Expansão da Agricultura Irrigada e Mudanças nos
704 Processos de Interação Superfície-Atmosfera: Um Estudo Numérico de Impacto Ambiental em
705 Áreas de Caatinga. *Rev. Bras. Geogr. Fís.*, 7, 960–968.

706 Miranda, R. Q., NÓBREGA, R. L. B., Moura, M. S. B., Raghavane, S., Galvíncio, J. D. (2020).
707 Realistic and simplified models of plant and leaf area indices for a seasonally dry tropical
708 forest. *Int. J. Appl. Earth Obs.*, 85, 1-9.

709 Muñoz-Jiménez, J. C., Sobrino, J. A., Gillespie, A., Sabol, D., Gustafson, W. T. (2006). Improved
710 land surface emissivities over agricultural areas using ASTER NDVI. *Remote Sens. Environ.*,
711 103, 474-487. <https://doi.org/10.1016/j.rse.2006.04.012>.

712 Oliveira, G. M., Leitão, M. M. V. B. R. L. (2000). Estimativas de evapotranspiração e as
713 consequências devido aos erros na determinação de saldo de radiação e efeitos advectivos. *Rev.*
714 *Bras. Eng. Agríc. Ambient.*, 4, 343-347.

715 Prata, A. J. (1996). A new long-wave formula for estimating downwelling clear-sky radiation at the
716 surface. *Q. J. R. Meteorol. Soc.*, 122, 1127-1151. <https://doi.org/10.1002/qj.49712253306>.

717 Priestley, C. H. B., Taylor, R. J. (1972). On the assessment of surface heat flux and evaporation using
718 large scale parameters. *Mon. Wea. Rev.* 100, 81–92. [http://dx.doi.org/10.1175/1520-0493\(1972\)100<0081:OTAOSH>2.3.CO;2](http://dx.doi.org/10.1175/1520-0493(1972)100<0081:OTAOSH>2.3.CO;2).

720 Projeto MapBiomass – Collection 3.1 from Annual Series of Brazilian coverage and land use maps.
721 Available at: <<http://mapbiomas.org/>>. (last accessed on 08 Jul 2019).

722 QGIS API. (2020). QGIS API Documentation. <https://qgis.org/api/3.6/>. Accessed Apr 2020.

723 Reynolds, M.K., Walker, D.A., Maier, H.A., 2006. NDVI patterns and phytomass distribution in the
724 circumpolar Arctic. *Remote Sens. Environ.* 102, 3–4, 271–281.
725 <http://dx.doi.org/10.1016/j.rse.2006.02.016>

726 Robinson, N.P.; Allred, B.W.; Jones, M.O.; Moreno, A.; Kimball, J.S.; Naugle, D.E.; Erickson, T.A.;
727 Richardson, A.D. (2017). A Dynamic Landsat Derived Normalized Difference Vegetation
728 Index (NDVI) Product for the Conterminous United States. *Remote Sens.*, 9, 1-14.
729 <https://doi.org/10.3390/rs9080863>.

730 Rouse, J.W, Haas, R.H., Scheel, J.A., and Deering, D.W. (1974). Monitoring Vegetation Systems in
731 the Great Plains with ERTS. Proceedings, 3rd Earth Resource Technology Satellite (ERTS)
732 Symposium, vol. 1, p. 48-62.
733 <https://ntrs.nasa.gov/archive/nasa/casi.ntrs.nasa.gov/19740022592.pdf>

734 Ruhoff, A., Paz, A. R., Collischonn, W., Aragao, L., Rocha, H., & Malhi, Y. (2012). A MODIS based
735 energy balance to estimate evapotranspiration for clear-sky days in Brazilian tropical savannas.
736 *Rem. Sens.*, 4, 703–725. <https://doi.org/10.3390/rs4030703>.

737 Ryu, Y., Kang, S., Moon, S. K., Kim, J. (2008). Evaluation of land surface radiation balance derived
738 from moderate resolution imaging spectroradiometer (MODIS) over complex terrain and
739 heterogeneous landscape on clear sky days. *Agric. For. Meteorol.*, 148, 1538-1552.
740 <https://doi.org/10.1016/j.agrformet.2008.05.008>.

741 Santos, C.A.C., Mariano, D.A., Nascimento, F.C.A., Dantas, F.R.C., Oliveira, G., Silva, M.T., Silva,
742 L.L., Silva, B.B., Bezerra, B.G., Safa, B., Medeiros, S.S., Neale, C.M.U., 2020. Spatio-
743 temporal patterns of energy exchange and evapotranspiration during an intense drought for
744 drylands in Brazil. *International Journal of Applied Earth Observation and Geoinformation* 85,
745 101982. <https://doi.org/10.1016/j.jag.2019.101982>

746 Santos, C. A. C., Silva, B. B. da, Rao, T. V. R., Satyamurti, P., Manzi, A. O. (2011). Downwelling
747 longwave radiation estimates for clear-sky conditions over Northeast Brazil. *Rev. Bras.*
748 *Meteorol*, 26, 443 – 450. <http://dx.doi.org/10.1590/S0102-77862011000300010>.

749 Silva, B. B. da, Braga, A. C., Braga, C. C. (2011). Balanço de radiação no perímetro irrigado São
750 Gonçalo – PB mediante imagens orbitais. *Rev. Caatinga*, 24, Mossoró, 145-152.

751 Silva, B. B., Montenegro, S. M. G. L., Silva, V. d. P. R., Rocha, H. R., Galvencio, J. D., and Oliveira,
752 L. M. M. (2015). Determination of instantaneous and daily net radiation from TM—Landsat 5
753 data in a subtropical watershed. *J. Atmos. Sol-Terr. Phy.*, 135, 42–49.
754 <https://doi.org/10.1016/j.jastp.2015.09.020>.

755 Silva, B.B. da, Braga, A. C., Braga, C. C., Oliveira, L. M. M. de, Montenegro, S.M.G.L., Barbosa
756 Junior, B. (2016). Procedures for calculation of the albedo with OLI-Landsat 8 images:
757 application to the Brazilian semiarid. *Rev. Bras. Eng. Agríc. Ambient.*, 20, 3-8.
758 <http://dx.doi.org/10.1590/1807-1929/agriambi.v20n1p3-8>.

759 Silva, J.M.C., Leal, I.R., Tabarelli, M. (2017). *Caatinga: The Largest Tropical Dry Forest Region in*
760 *South America*. Springer International Publishing, Cham, Switzerland, [https:](https://doi.org/10.1007/978-3-319-68339-3)
761 [//doi.org/10.1007/978-3-319-68339-3](https://doi.org/10.1007/978-3-319-68339-3).

762 Silveira, H. L. F., Galvão, L. S., Sanches, I. D. A., Sá, I. B., Taura, T. A. (2018). Use of MSI/Sentinel-
763 2 and airborne LiDAR data for mapping vegetation and studying the relationships with soil
764 attributes in the Brazilian semi-arid region. *Int. J. Appl. Earth Obs. Geoinf*, 73, 179–190.
765 <https://doi.org/10.1016/j.jag.2018.06.016>

766 Sugita, M., Brutsaert, W. H. (1993). Cloud effect in the estimation of instantaneous downwelling
767 longwave radiation. *Water Resour. Res.*, 29, 599–605. <https://doi.org/10.1029/92WR02352>.

768 Swinbank, W. C. (1963). Long-wave radiation in from clear skies. *Q. J. R. Meteorol. Soc.*, 89, 339-
769 348. <https://doi.org/10.1002/qj.49708938105>.

770 Tang, B., Li, Z. L. (2008). Estimation of instantaneous net surface longwave radiation from MODIS
771 cloud-free data. *Remote Sens. Environ.*, 112, 3482-3492.
772 <https://doi.org/10.1016/j.rse.2008.04.004>.

773 Tasumi, M. (2003). Progress in Operational Estimation of Regional Evapotranspiration Using
774 Satellite Imagery. Ph.D. dissertation. University of Idaho, Moscow, ID.

775 Teixeira, A. H. C., Bastiaanssen, W. G. M., Ahmad, M. D., Bos, M. G. (2009). Reviewing SEBAL
776 input parameters for assessing evapotranspiration and water productivity for the Low-Middle
777 São Francisco River basin, Brazil - Part A: calibration and validation. *Agric. For. Meteorol.*
778 149, 462-476. <https://doi.org/10.1016/j.agrformet.2008.09.016>.

779 Teixeira, A. H. C., Bastiaanssen, W. G. M., Ahmad, M. D., Moura, M. S. B., Bos, M. G. (2008).
780 Analysis of energy fluxes and vegetation-atmosphere parameters in irrigated and natural
781 ecosystems of semi-arid Brazil. *J. Hydrol.*, 362, 110-127.
782 <https://doi.org/10.1016/j.jhydrol.2008.08.011>

783 Trigo, I. F., de Bruin, H., Beyrich, F., Bosveld, F. C., Gavián, P., Groh, J., López-Urrea, R. (2018).
784 Validation of reference evapotranspiration from Meteosat Second Generation (MSG)
785 observations. *Agric. Forest Meteorol.* 259, 271–285.
786 <https://doi.org/10.1016/j.agrformet.2018.05.008>.

787 Urrutia, A. L., González-González, C., Van Cauwelaert, E. M., Rosell, J. A., García Barrios, L.,
788 Benítez, M. (2020). Landscape heterogeneity of peasant-managed agricultural matrices. *Agric.*
789 *Ecosyst. Environ.* 292, 106797. <https://doi.org/10.1016/j.agee.2019.106797>.

790 USGS - United States Geological Survey. Landsat Update. Vol. 7 Issue 5, Available at:
791 <https://landsat.usgs.gov/sites/default/files/documents/about_LU_Vol_7_Issue_5.pdf>. (last
792 accessed on 24 Jul 2018).

793 Vancoppenolle, M., Fichefet, T., Goosse, H., Bouillon, S., Madec, G., Morales Maqueda, M. A.
794 (2009). Simulating the mass balance and salinity of Arctic and Antarctic sea ice. 1: Model
795 description and validation. *Ocean Modell.* 27, 33–53.
796 <https://doi.org/10.1016/j.dsr2.2010.10.039>.

797 Verhoef, A. and Campbell, C.L. (2005) Evaporation Measurement, Ch. 40. In: *Encyclopedia of*
798 *Hydrological Sciences* Vol. 1. Editor: M.G. Anderson. John Wiley, Chichester, UK: 589-601.

799 Waldmann-Selsam, C., Balmori-de la Puente, A., Breunig, H., Balmori, A. (2016). Radiofrequency
800 radiation injures trees around mobile phone base stations, *Sci. Total Environ.* 572, 554–569.
801 <https://doi:10.1016/j.scitotenv.2016.08.045>.

802 Wang, W., Liang, S. (2009). Estimation of high-spatial resolution clear-sky longwave downwelling
803 and net radiation over land surfaces from MODIS data. *Remote Sens. Environ.*, 113, 745–754.
804 <https://doi.org/10.1016/j.rse.2008.12.004>.

805 Wang, Y.P., Li, R., Min, Q, Fu, Y, Wang, Y., Zhong, L., and Fu, Y.-Y. (2019). A Three-source
806 Satellite Algorithm for Retrieving All-sky Evapotranspiration Rate using Combined Optical
807 and Microwave Vegetation Index at Twenty Asia Flux Sites, *Remote Sens. Environ.*, 235,
808 111463, <https://doi.org/10.1016/j.rse.2019.111463>.

809 Wijesingha, J., Moeckel, T., Hensgen, F., Wachendorf, M. (2019). Evaluation of 3D point cloud-
810 based models for the prediction of grassland biomass. *Int. J. Appl. Earth Obs. Geoinf.* 78, 352–
811 359. <https://doi.org/10.1016/j.jag.2018.10.006>.

812 WMO. (1989). Calculation of Monthly and Annual 30-Year Standard Normals, WCDP-No. 10,
813 WMOTD/No. 341. World Meteorological Organization: Geneva.

814

815 Zhu W., Jia, S., Lv, A. 2017. W. Zhu, S. Jia, A. Lv. (2017). A time domain solution of the Modified
816 Temperature Vegetation Dryness Index (MTVDI) for continuous soil moisture monitoring.
817 Remote Sens. Environ., 200, pp. 1-17. <https://doi.org/10.1016/j.rse.2017.07.032>

818 Zillman, J. W. (1972). A study of some aspects of the radiation and heat budgets of the southern
819 hemisphere oceans, meteorological study 26. Canberra, Australia: Commonwealth Bureau of
820 Meteorology.